THE ASTROPHYSICAL JOURNAL, 950:13 (20pp), 2023 June 10 https://doi.org/10.3847/1538-4357/acc4bb

Observable Signature of Merging Stellar-mass Black Holes in Active Galactic Nuclei

Hiromichi Tagawa[1,2,3], Shigeo S. Kimura[2,4], Zoltán Haiman[1], Rosalba Perna[5,6], and Imre Bartos[7]
[1] Department of Astronomy, Columbia University, 550 W. 120th St., New York, NY 10027, USA; ht2613@columbia.edu
[2] Astronomical Institute, Graduate School of Science, Tohoku University, Aoba, Sendai 980-8578, Japan
[3] National Astronomical Observatory of Japan, National Institutes of Natural Sciences, 2-21-1 Osawa, Mitaka, Tokyo 181-8588, Japan
[4] Frontier Research Institute for Interdisciplinary Sciences, Tohoku University, Sendai 980-8578, Japan
[5] Department of Physics and Astronomy, Stony Brook University, Stony Brook, NY 11794-3800, USA
[6] Center for Computational Astrophysics, Flatiron Institute, New York, NY 10010, USA
[7] Department of Physics, University of Florida, PO Box 118440, Gainesville, FL 32611, USA

Received 2023 January 17; revised 2023 March 14; accepted 2023 March 14; published 2023 June 6

Abstract

The origin of stellar-mass black hole mergers discovered through gravitational waves is being widely debated. Mergers in the disks of active galactic nuclei (AGNs) represent a promising source of origin, with possible observational clues in the gravitational-wave data. Beyond gravitational waves, a unique signature of AGN-assisted mergers is electromagnetic emission from the accreting black holes. Here we show that jets launched by accreting black holes merging in an AGN disk can be detected as peculiar transients by infrared, optical, and X-ray observatories. We further show that this emission mechanism can explain the possible associations between gravitational-wave events and the optical transient ZTF 19abanrhr and the proposed gamma-ray counterparts GW150914-GBM and LVT151012-GBM. We demonstrate how these associations, if genuine, can be used to reconstruct the properties of these events' environments. Searching for infrared and X-ray counterparts to similar electromagnetic transients in the future, once host galaxies are localized by optical observations, could provide a smoking-gun signature of the mergers' AGN origin.

Unified Astronomy Thesaurus concepts: Gravitational wave sources (677); High energy astrophysics (739); Black hole physics (159); Active galactic nuclei (16); Jets (870); Transient sources (1851); Time domain astronomy (2109)

1. Introduction

Despite the large number of black hole mergers discovered by the LIGO (LIGO Scientific Collaboration et al. 2015), Virgo (Acernese et al. 2015), and KAGRA (Akutsu et al. 2021) gravitational-wave observatories (The LIGO Scientific Collaboration et al. 2021), the astrophysical pathways to these mergers are still debated. A promising environment for mergers is the disk of an active galactic nucleus (AGN; Bartos et al. 2017; Stone et al. 2017; McKernan et al. 2020; Tagawa et al. 2020b). Theory and observations (Artymowicz et al. 1993; Levin & Beloborodov 2003; Tagawa et al. 2020b; Fan & Wu 2023) suggest that black holes get embedded in AGN disks due to capture via dynamical interactions between the nuclear star cluster and the AGN disk (Ostriker 1983; Miralda-Escudé & Kollmeier 2005) and by in situ star formation (Levin & Beloborodov 2003; Milosavljević & Loeb 2004). The AGN disks then act as black hole assembly lines (Cheng & Wang 1999), bringing the black holes closer together and helping them merge over relatively short timescales. It is also possible that multiple black holes merge consecutively, resulting in unusually heavy remnants (Yang et al. 2020; Tagawa et al. 2021a). Comparisons to the observed black hole masses, spins, and merger rate indicate that a sizable fraction of the observed mergers may originate in AGNs (Gayathri et al. 2021; Tagawa et al. 2021a; Ford & McKernan 2022). The AGNs could also explain some of the peculiar detections, such as those with a high mass (Tagawa et al. 2021a) and possible high eccentricity (Romero-Shaw et al. 2020, 2022; Tagawa et al. 2021b; Gayathri et al. 2022; Samsing et al. 2022).

Due to the gas-rich merger environment, a key signature of the AGN channel is the possibility of electromagnetic emission accompanying the gravitational-wave signal from the merger (Bartos et al. 2017; Stone et al. 2017). To explore this possibility, electromagnetic follow-up observations have been carried out for many of the mergers, with nine counterparts suggested so far. These include the peculiar optical flare ZTF 19abanrhr, with luminosity $L \sim 10^{45}\,\mathrm{erg\,s^{-1}}$ and duration $t_{\mathrm{duration}} \sim 1$ month, detected by the Zwicky Transient Facility (ZTF) in the AGN J124942.3+344929. It was observed in spatial coincidence with and within 18 days of GW190521 (Graham et al. 2020; Calderón Bustillo et al. 2021), the heaviest black hole merger detected to date (Abbott et al. 2020a). Recently, six optical flares possibly associated with massive black hole mergers with luminosity and duration similar to those of ZTF 19abanrhr were additionally reported by Graham et al. (2023). The first gravitational-wave event, GW150914 (Abbott et al. 2016a), has also been proposed to have an associated bright gamma-ray event detected by the Fermi Gamma-ray Burst Monitor (GBM), GW150914-GBM (Connaughton et al. 2016, 2018), with $L \sim 10^{49}\,\mathrm{erg\,s^{-1}}$ and $t_{\mathrm{duration}} \sim 1$ s (but see Greiner et al. 2016; Savchenko et al. 2016). Finally, another gamma-ray burst candidate has been associated with the tentative gravitational-wave event, LVT151012 (Bagoly et al. 2016), with properties similar to those of GW150914-GBM. As these associations remain debated and controversial (Greiner et al. 2016; Savchenko et al. 2016; Calderón Bustillo et al. 2021), it is necessary to consider whether a self-consistent physical model can, in fact, explain all of the properties of these tentative associations.

The possibility of electromagnetic emission from merging black holes in AGN disks has been actively studied recently, mainly focusing on optical flares (McKernan et al. 2019; Graham et al. 2020; Kimura et al. 2021; Wang et al. 2021). Additionally, multiple scenarios have been proposed to

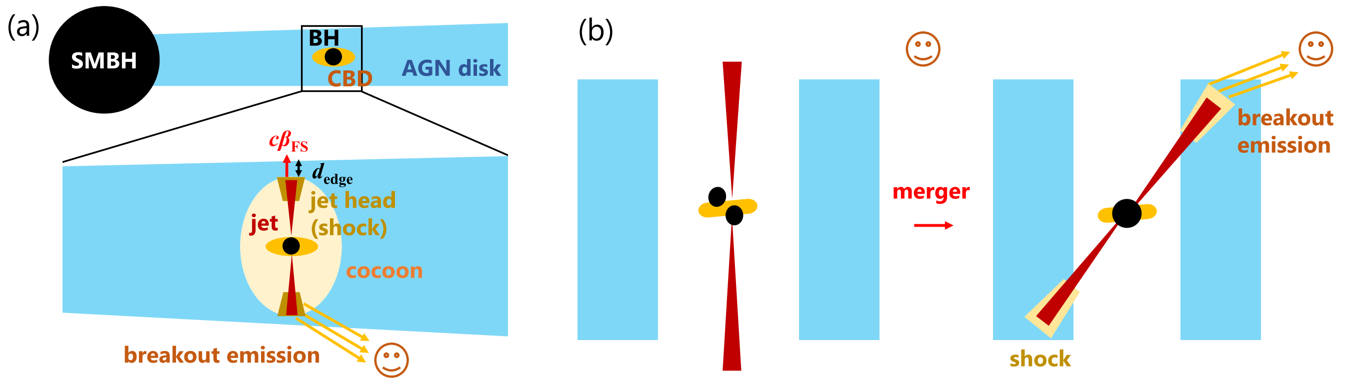

Figure 1. Schematic pictures of the breakout emission. (a) Breakout emission from the head of a jet launched from a solitary black hole embedded in an AGN disk. From a solitary black hole, the breakout emission is produced episodically, after replenishment of gas to the black hole (Tagawa et al. 2022). (b) Emission from shocks produced around a jet after a merger. The jet direction is aligned with the black hole spin direction or the angular momentum direction of a circum-black hole disk, which is reoriented by the merger. As a result, the jet again collides with unshocked AGN gas, producing breakout emission after the merger.

produce emission similar to GW150914-GBM in more generic galactic environments (e.g., Perna et al. 2016; Janiuk et al. 2017). However, no model has been able to explain all of the properties, including the luminosity, delay time, duration, and color of electromagnetic transients. Furthermore, ZTF 19abanrhr began brightening only approximately 18 days after the merger, which has not been physically justified (see Section 3.3.2).

A promising process for the production of detectable electromagnetic emission from AGN-assisted black hole mergers is the launch of a relativistic jet through the Blandford–Znajek effect (Tagawa et al. 2022; see Figure 1 for a schematic illustration). We evaluated the properties and observability of nonthermal and thermal emission from shocks emerging around such jets. In the AGN disk, a black hole is often surrounded by a circum–black hole disk (Tagawa et al. 2022). When the circum–black hole disk is advection dominated, as realized in the slim disk model expected in this environment (Abramowicz et al. 1988), a magnetically dominated state can be realized owing to the accumulation of magnetic flux in the vicinity of the black hole (Cao 2011; the magnetic field can be further magnified by an outflow; see, e.g., Liska et al. 2020). In such cases, a jet is expected to be launched from a spinning black hole via the Blandford–Znajek process (Blandford & Znajek 1977).

As the jet collides with unshocked gas in the AGN disk, strong forward and reverse shocks are formed in the disk and the jet head, respectively, and shocked material surrounds the sides of the jet (cocoon). During the early phases, photons in the shocked medium cannot escape from the system because they are surrounded by an optically thick disk. As the shock approaches the surface of the AGN disk, photons begin escaping from the system, leading to luminous thermal and nonthermal emission (Figure 1(a)). Note that solitary black holes produce similar breakout emission, but it will be difficult to observe because of lower brightness compared to that from merging black holes and the low duty cycle of the breakout emission (Tagawa et al. 2023); the jet self-regulates to an episodic behavior by creating a cavity around the black hole, with the breakout emission existing only for a small fraction of each cycle (Kimura et al. 2021; Tagawa et al. 2022). On the other hand, we show that breakout emission from merging black holes is expected to be observable due to its brightness and that it accompanies up to several percent of black hole mergers in these environments (see Section 4.1). We further present a prescription for how nonthermal and thermal emission from these shocks can be used to "reverse engineer" the properties of the merger environments, applying the technique to the transients proposed to be associated with black hole mergers: ZTF 19abanrhr, GW150914-GBM, and LVT151012-GBM.

2. Model Description

In this section, we describe our model of accretion onto black holes, the properties of thermal and nonthermal emission, and our numerical choices. The various parameters of our model are summarized in Tables 1 and 2 in Appendix A. Readers not interested in the model details may skip directly to the next section, describing our results.

2.1. Accretion onto Black Holes

A Blandford–Znajek jet is expected to be launched from rapidly accreting and spinning black holes in an AGN disk, as we outlined in Appendix A.1 of Tagawa et al. (2022). The jet kinetic luminosity ($L_{\rm j}$) is proportional to the mass accretion rate onto the black hole ($\dot{m}$),

$$L_{\rm j} = \eta_{\rm j} \dot{m} c^2, \tag{1}$$

where $\eta_{\rm j}$ is the jet conversion efficiency, which is approximated by $\eta_{\rm j} \sim a_{\rm BH}^2$ for a magnetically dominated jet (Tchekhovskoy et al. 2010; Narayan et al. 2022), and $a_{\rm BH}$ is the dimensionless spin of the black hole. Since the power of the shock emerged around the jet and the luminosity of radiation emitted from the shock are roughly proportional to the jet kinetic luminosity, the accretion rate onto the black hole is a key quantity to determine the observed luminosity from the system.

The accretion rate onto a circum–black hole disk in the AGN disk is evaluated via the Bondi–Hoyle–Lyttleton rate, as given by Equation (1) of Tagawa et al. (2022). By considering the reduction from the Bondi–Hoyle–Lyttleton rate, we parameterized the fraction of the accretion rate onto the black hole ($\dot{m}$) over the Bondi–Hoyle–Lyttleton rate ($\dot{m}_{\rm BHL}$) as $f_{\rm acc} = \dot{m}/\dot{m}_{\rm BHL}$. For example, low $f_{\rm acc}$ may be predicted due to winds from an accretion disk with a super-Eddington rate, although recent simulations suggest that the conversion to wind is moderate (Kitaki et al. 2021) for accretion flows onto black holes in an AGN disk, in which the circularization radius is much larger than the trapping radius. In addition, the accretion

Table 1
Fiducial Values of Our Model Parameters and Their Influence on the Properties of the Breakout Emission

Parameter	Fiducial Value	Sensitivity to Results
Radial distance of the black hole from the supermassive black hole	$R = 2.5$ pc	Very sensitive on the three properties
Ratio of the black hole accretion rate to the gas capture rate	$f_{\rm acc} = 15$	Sensitive on $L_{\rm breakout}$ and moderate on $t_{\rm delay}$ and $t_{\rm duration}$
Conversion efficiency of shock kinetic energy to magnetic/electron energy	$\epsilon_{\rm B} = 0.1$, $\epsilon_{\rm e} = 0.3$	Very sensitive on reducing $L_{\rm nonthermal}$
Jet energy conversion efficiency	$\eta_{\rm j} = 0.5$	Sensitive on $L_{\rm breakout}$ and moderate on $t_{\rm delay}$ and $t_{\rm duration}$ but constrained
Mass of the merged remnant	$m = 150\,M_\odot$	Sensitive on $L_{\rm breakout}$ and moderate on $t_{\rm delay}$ and $t_{\rm duration}$ but constrained
Gas inflow rate from the outer boundary of the AGN disk	$\dot{M}_{\rm in} = 50\,L_{\rm Edd}/c^2$	Sensitive on the three properties but constrained
Mass of the supermassive black hole	$M = 10^8\,M_\odot$	Sensitive on the three properties but constrained
Opening angle at the base of the jet	$\theta_0 = 0.3$	Moderate on the three parameters
Angular momentum transfer parameter in outer regions of the AGN disk	$m_{\rm AM} = 0.5$	Moderate on the three parameters
Viscous parameter of the AGN disk	$\alpha_{\rm AGN} = 0.1$	Insensitive on the three parameters

Note. For sensitivity, we made a rough classification of the parameters influencing the results ($L_{\rm breakout}$, $t_{\rm delay}$, and $t_{\rm duration}$) by more than 2 orders of magnitude ("very sensitive"), 1 order of magnitude ("sensitive"), a factor of $\gtrsim 2$ ("moderate"), and a factor of $\lesssim 2$ ("insensitive"). We also add the comment "constrained" for parameters that are well constrained by the observations of ZTF 19abanrhr.

rate onto the black hole in a cavity in active phases is estimated to be lower by a factor of a few compared to that without a cavity (Tagawa et al. 2022). On the other hand, for merger remnants, inflow rates can be enhanced by shocks arising in the marginally bound annuli of the postmerger circum–black hole disks due to recoil kicks imparted on the remnants. Considering this process, we adopt $f_{\rm acc} = 15$ as a fiducial value, as discussed in detail in Appendix B.

2.2. Thermal Emission at Breakout

Here we provide details on the mechanisms involved in the production of thermal emission from shocks produced by the interaction between the AGN disk and the jet launched from the accreting black holes. We consider emission from the shocks propagating in optically thick media (an AGN disk; Figure 1). We assume that the black hole is at the midplane of the AGN disk, and the jet direction is perpendicular to the AGN disk plane. On the other hand, if the jet is inclined with respect to the angular momentum direction of the AGN disk by an angle i, the distance to the surface of the AGN disk from the black hole needs to be enhanced by a factor of $1/\cos(i)$ compared to the estimates in this paper, while other modifications would be minor. While the diffusion of photons is slower than the propagation of a shock, $v_{\rm FS} = \beta_{\rm FS} c > c/\tau$, where τ is the optical depth of the AGN disk, and $v_{\rm FS} = \beta_{\rm FS} c$ is the velocity of the forward shock, photons are trapped in the shock. Once the shock propagates to the height at which the diffusion to the edge (the disk photosphere) becomes faster than the propagation ($\beta_{\rm FS} c < c/\tau$), photons start to escape. The observed properties (such as temperature, duration, and luminosity) of the emission from the shock breakout are differently characterized depending on the ranges of the shock velocity (Figure 2), as described in the following (Ito et al. 2020; Levinson & Nakar 2020).

For Newtonian shocks with $\beta_{\rm FS}\gamma_{\rm FS} \lesssim 0.03$ (Nakar & Sari 2010; Sapir et al. 2013), where $\gamma_{\rm FS}$ is the Lorentz factor of the forward shock, the radiation is in thermodynamic equilibrium, as there is time to emit a sufficient number of photons by free–free emission. From the jump condition for a strong shock, the thermal equilibrium temperature is

$$T_{\rm breakout} \sim (18\rho_{\rm AGN} v_{\rm FS}^2/7a)^{1/4} \sim 10^4\,{\rm K}\left(\frac{\beta_{\rm FS}}{0.02}\right)^{1/2}\left(\frac{\rho_{\rm AGN}}{1\times 10^{-16}\,{\rm g\,cm^{-3}}}\right)^{1/4}, \tag{2}$$

where a is the radiation constant, and $\rho_{\rm AGN}$ is the density of the AGN disk. The breakout emission typically peaks in the optical or UV bands, $E_{\gamma,{\rm BO}} \sim 2.8\,k_{\rm B} T_{\rm breakout} \sim 1$–$100$ eV, where $k_{\rm B}$ is the Boltzmann constant.

In the nonrelativistic regime, photons inside the shock start to diffuse out from the AGN disk when the photon diffusion time, $t_{\rm diff} \sim d_{\rm edge}^2 \kappa_{\rm AGN} \rho_{\rm AGN}/c$, becomes equal to the shock expansion time, $t_{\rm dyn} \sim d_{\rm edge}/v_{\rm FS}$, where $d_{\rm edge}$ is the thickness of the AGN disk above the shock, and $\kappa_{\rm AGN}$ is the opacity of the AGN disk for thermal photons. By equating the timescales, the thickness at the breakout is given by $d_{\rm edge,BO} \sim c/(v_{\rm FS}\kappa_{\rm AGN}\rho_{\rm AGN})$, and the duration of emission from a breakout shell is

$$t_{\rm breakout} \sim c/(v_{\rm FS}^2 \kappa_{\rm AGN} \rho_{\rm AGN}) \sim 3\,{\rm yr}\left(\frac{\beta_{\rm FS}}{0.1}\right)^{-2}\left(\frac{\rho_{\rm AGN}}{1\times 10^{-16}\,{\rm g\,cm^{-3}}}\right)^{-1}, \tag{3}$$

where we adopt the Thomson scattering opacity of $\kappa_{\rm AGN} \sim 0.4\,{\rm g\,cm^{-2}}$ assuming ionized gas. The observed duration for bright emission ($t_{\rm duration}$) is typically given by $t_{\rm breakout}$ in nonrelativistic cases. The luminosity roughly evolves following $L \propto e^{t^2}$ (Sapir et al. 2011) and $L \propto t^{-4/3}$ before and after breakout during a planar phase ($t < t_{\rm sph}$), respectively, where $t_{\rm sph} = H_{\rm AGN}/v_{\rm FS}$ is the time of transition between the planar and spherical geometries of the breakout shell after the breakout of the shock, and $H_{\rm AGN}$ is the scale height of the AGN disk. The dependence of the time evolution of the luminosity on the density profile of the ambient material is found to be weak (Sapir et al. 2011). After $t_{\rm sph}$, the luminosity evolves more modestly depending on the preshocked density profile. Note that for simplicity, we adopt formulae obtained in a spherical geometry, while the evolution of the breakout luminosity from shocks propagating in a disk geometry would require modification from them (Grishin et al. 2021).

The delay time between the production of a jet and the breakout is roughly given by

$$t_{\rm break} \sim \frac{3}{5}\frac{H_{\rm AGN}}{v_{\rm FS}} \sim 0.3\ {\rm yr}\left(\frac{H_{\rm AGN}}{5\times10^{16}\ {\rm cm}}\right)\left(\frac{\beta_{\rm FS}}{0.1}\right)^{-1}, \tag{4}$$

where the prefactor of $3/5$ accounts for the deceleration during the nonrelativistic regime. The time delay between the gravitational wave and the breakout emission ($t_{\rm delay}$) is roughly given by $t_{\rm break}$ in nonrelativistic regimes. Note that $t_{\rm delay}$ can be lowered compared to $t_{\rm break}$ by up to the breakout timescale of gravitational waves ($t_{\rm GW,break} \sim H_{\rm AGN}/c$) if the line-of-sight and jet-propagating directions coincide. This is because the breakout emission is produced closer to us in such cases compared to those for random jet directions.

The breakout luminosity of the thermal emission ($L_{\rm breakout}$) and the kinetic power of the shock ($L_{\rm sh}$) are typically (Nakar & Sari 2010)

$$\begin{aligned} L_{\rm breakout} \sim L_{\rm sh} &\sim \pi\theta_{\rm j}^2 H_{\rm AGN}^2 \rho_{\rm AGN} v_{\rm FS}^3 \\ &\sim 5\times10^{43}\ {\rm erg\ s^{-1}}\left(\frac{\theta_{\rm j}}{0.05}\right)^2 \\ &\times\left(\frac{H_{\rm AGN}}{5\times10^{16}\ {\rm cm}}\right)^2\left(\frac{\rho_{\rm AGN}}{1\times10^{-16}\ {\rm g\ cm^{-3}}}\right)\left(\frac{\beta_{\rm FS}}{0.1}\right)^3, \end{aligned} \tag{5}$$

where $\theta_{\rm j}$ is the opening angle of the jet, which is given by $\theta_{\rm j} \sim (L_{\rm j}\theta_0^6\beta_{\rm FS}^2/\rho_{\rm AGN}H_{\rm AGN}^2c^3)^{1/10}$ for nonrelativistic regimes (Bromberg et al. 2011).

For Newtonian shocks with $0.03 \lesssim \beta_{\rm FS}\gamma_{\rm FS} \lesssim 1$, the breakout temperature ($T_{\rm breakout}$) strongly depends on the shock velocity (Budnik et al. 2010; Sapir et al. 2013). In these regimes, since the number of photons produced by free–free emission during propagation is lower than that required to establish thermal equilibrium (Nakar & Sari 2010), the radiation is out of thermodynamic equilibrium, and the photons roughly follow the local Compton equilibrium, whose radiation is characterized by a Wien spectrum $de_{\rm ph}/d\nu \propto \nu^3 {\rm e}^{-h\nu/k_{\rm B}T_{\rm breakout}}$, where ν and $e_{\rm ph}$ are the frequency and spectral energy density of photons, and h is the Planck constant. The breakout temperature of the photons is calculated and fitted as (Sapir et al. 2013)

$$\begin{aligned} \log_{10}\left(\frac{T_{\rm breakout}}{10^4\ {\rm K}}\right) &= 0.975 + 1.735\left(\frac{\beta_{\rm FS}}{0.1}\right)^{1/2} \\ &+ \left[0.26 - 0.08\left(\frac{\beta_{\rm FS}}{0.1}\right)^{1/2}\right]\log_{10}\left(\frac{n_{\rm AGN}}{10^{15}\ {\rm cm^{-3}}}\right), \end{aligned} \tag{6}$$

where $n_{\rm AGN} = \rho_{\rm AGN}/m_{\rm p}$ is the number density of the AGN disk gas, and $m_{\rm p}$ is the proton mass. Note that this formula likely somewhat underestimates $T_{\rm breakout}$ for high $\beta_{\rm FS}$ and flat density profiles (roughly up to a factor of a few; Figure 3 in Sapir et al. 2013).

The duration of the breakout emission ($t_{\rm duration}$), the breakout timescale ($t_{\rm break}$), and the kinetic power of the shock ($L_{\rm sh}$) in the fast-Newtonian regimes are given by Equations (3)–(5) as in the slow-Newtonian regimes.

We follow Nakar & Sari (2012) to model evolution in relativistic regimes. For relativistic shocks with $\beta_{\rm FS}\gamma_{\rm FS} \gtrsim 1$, electron/positron pairs are abundantly created, which enhances the production of photons inside the shock and regulates the temperature in the rest frame of the downstream plasma to ∼100–200 keV, almost independent of $\beta_{\rm FS}$ (Budnik et al. 2010). Here the relativistic shells are accelerated from the initial Lorentz factor of $\gamma_{\rm FS}$ to $\gamma_{\rm FS,f} = \gamma_{\rm FS}^{1+\sqrt{3}}$ due to the decrease of the gas density before breakout for $\gamma_{\rm FS} \lesssim 4$ (Johnson & McKee 1971), which is satisfied below. Note that breakout emission for $\gamma_{\rm FS} \gtrsim 4$ is not well investigated, and the applicability of the formalism is unclear. We also assume that the observer is within the angle of $\lesssim 1/\gamma_{\rm sf,f}$ from the direction of the shock propagation, and that radiation is beamed unless stated otherwise, where $\gamma_{\rm sf,f} \approx \gamma_{\rm sf}^{1+\sqrt{3}}$ is the final Lorentz factor of the shocked fluid, $\gamma_{\rm sf}$ is the initial Lorentz factor of the shocked fluid, and $\gamma_{\rm FS} \sim \sqrt{2}\,\gamma_{\rm sf}$ for strong shocks in relativistic regimes.

The delay time between a jet launch and the breakout from the AGN disk is roughly given by

$$t_{\rm delay} \sim \max\,(t_{\rm break,rel},\, t_{\rm trans}), \tag{7}$$

where

$$t_{\rm break,rel} = \frac{H_{\rm AGN}}{4\gamma_{\rm FS}^2 c} \tag{8}$$

is the breakout timescale of the shock in relativistic regimes, in which the factor of $1/2$ accounts for the deceleration during Blandford–McKee phases (Blandford & McKee 1976), and the factor of $H_{\rm AGN}/(2\gamma_{\rm FS}^2 c)$ approximately accounts for the difference between the apparent travel time of the gravitational waves and the forward shock ($\sim H_{\rm AGN}/(\beta_{\rm FS}c) - H_{\rm AGN}/c$). Here $t_{\rm trans}$ is the time at which the breakout shell with a temperature of $k_{\rm B}T_{\rm breakout} \sim 200\ {\rm keV}\ \gamma_{\rm sf,f}$ in the shock immediately downstream becomes optically thin by the annihilation of pairs at a temperature of

$$k_{\rm B}T_{\rm breakout} \sim 50\ {\rm keV}\ \gamma_{\rm sf,f} \tag{9}$$

due to cooling of the shell by adiabatic expansion (we adopt Equation (13) of Nakar & Sari 2012). The timescale $t_{\rm trans}$ should be taken into account for relativistic regimes, since shocks are not transparent before the annihilation of pairs due to the enhancement of the optical depth by a factor of $\gtrsim$100.

The duration of the emission from the breakout shell is

$$t_{\rm duration} \sim \max\,(t_{\rm ang},\, t_{\rm trans},\, t_{\rm breakout}), \tag{10}$$

where

$$t_{\rm ang} = \frac{H_{\rm AGN}}{2\gamma_{\rm sf,f}^2 c} \tag{11}$$

is the timescale during which radiation emitted by the same shell is observed due to its round shape in the relativistic regime. In relativistic regimes and when shocks are propagating toward the observer, the breakout timescale ($t_{\rm breakout}$) is reduced due to the beaming effect by $\sim\gamma_{\rm FS}^2$, pair production by $100\,\gamma_{\rm FS}$, and the Klein–Nishina effect by $\gamma_{\rm FS}^{-2}$ (Budnik et al. 2010) as

$$t_{\rm breakout} \sim \frac{c}{100 v_{\rm FS}^2 \kappa_{\rm AGN} \rho_{\rm AGN} \gamma_{\rm FS}}. \tag{12}$$

For relativistic cases, the kinetic power of the shock is (Blandford & McKee 1976)

$$L_{\rm sh} \sim \pi \theta_{\rm j}^2 H_{\rm AGN}^2 \rho_{\rm AGN} v_{\rm FS} \gamma_{\rm FS}^2 c^2, \tag{13}$$

while the isotropic equivalent breakout luminosity is given by Nakar & Sari (2012),

$$L_{\rm breakout} \sim \pi f_{\rm beaming}\, \theta_{\rm j}^2 H_{\rm AGN}^2 \rho_{\rm AGN} v_{\rm FS} \gamma_{\rm FS}^2 c^2 \frac{\gamma_{\rm sf,f}}{4\gamma_{\rm sf}}, \tag{14}$$

where $f_{\rm beaming}$ is the beaming factor, taking into account the angular effect due to the fact that emission is concentrated in the direction of shock motion. We assume $f_{\rm beaming} = 2\gamma_{\rm sf,f}^2$ approximating that the radiation is concentrated within the angle $\sim 1/\gamma_{\rm sf,f}$ from the direction of the shock motion. Equation (13) includes an additional boosting factor to account for conversion of the emitted power to the observer frame to obtain the full Doppler boost. We assume that the breakout shell has a width of $v_{\rm FS} t_{\rm duration}$ (which is different from the width for the nonthermal emission of $v_{\rm FS} t_{\rm breakout}$). The factor of $\gamma_{\rm sf,f}/4\gamma_{\rm sf}$ in Equation (14) represents the reduction of the internal energy due to adiabatic expansion. The temperature in the immediate shock downstream is so high ($\sim$200 keV $\gamma_{\rm sf}$) that photons cannot escape from the shell because of copious electron/positron pairs. The photons escape from the shell after it expands and the temperature becomes $\sim$50 keV $\gamma_{\rm sf,f}$. Thus, the internal energy and luminosity of the thermal emission are reduced by a factor of $\gamma_{\rm sf,f}/4\gamma_{\rm sf}$.

In summary, we adopt Equations (2), (6), and (9) for $T_{\rm breakout}$ for $\beta_{\rm FS}\gamma_{\rm FS} \leqslant 0.03$, $1 \geqslant \beta_{\rm FS}\gamma_{\rm FS} \geqslant 0.03$, and $\beta_{\rm FS}\gamma_{\rm FS} \geqslant 1$, respectively. The radiation is roughly characterized by blackbody radiation and a Wien spectrum for $\beta_{\rm FS}\gamma_{\rm FS} \leqslant 0.03$ and $\geqslant 0.03$, respectively, although numerical simulations find that the spectrum at breakout is typically softer than that, especially for Newtonian slow shocks and in relativistic regimes (Budnik et al. 2010; Ito et al. 2020). Also, we assume that $t_{\rm delay}$ is given by Equations (4) and (7); $t_{\rm duration}$ is given by Equations (3) and (10) for $\beta_{\rm FS}\gamma_{\rm FS} \leqslant 1$ and $\geqslant 1$, respectively; and $L_{\rm sh}$ and $L_{\rm breakout}$ are given by Equation (5) for $\beta_{\rm FS}\gamma_{\rm FS} \leqslant 1$ and Equations (13) and (14), respectively, for $\beta_{\rm FS}\gamma_{\rm FS} \geqslant 1$.

The velocity of the shocked fluid ($\beta_{\rm sf}$) is determined by the competition between the power of the jet $L_{\rm j}$ and the mass of the ambient material swept up by the jet (Bromberg et al. 2011), which is derived using the density ($\rho_{\rm AGN}$), the scale height of the AGN disk ($H_{\rm AGN}$), and the injected opening angle of the jet ($\theta_{\rm j}$). Note that at the transitions where $\beta_{\rm sf}\gamma_{\rm sf} \sim 1$ or $\tilde{L} \sim 1$, where $\tilde{L}$ is the ratio between the energy density of the jet and the rest-mass energy density of the surrounding medium at the location of the head, the formulae in Bromberg et al. (2011) unexpectedly predict that $\beta_{\rm sf}\gamma_{\rm sf}$ decreases as $L_{\rm j}$ increases. To avoid this, we set the upper limit for $\tilde{L} \leqslant 1$ and the lower limit for $\tilde{L} \geqslant 1$ to be $\beta_{\rm sf}\gamma_{\rm sf} = 1$, since the two cases correspond to $\beta_{\rm sf} < 1$ (with $\gamma_{\rm sf} \sim 1$) and $\gamma_{\rm sf} > 1$ (with $\beta_{\rm sf} \sim 1$), respectively. Thus, $\beta_{\rm sf}\gamma_{\rm sf}$ is not accurately determined at around $\beta_{\rm sf}\gamma_{\rm sf} \sim 1$.

To model ZTF 19abanrhr, $\rho_{\rm AGN}$ and $H_{\rm AGN}$ are determined following the AGN disk model of Thompson et al. (2005) given the input parameters, gas inflow rate ($\dot{M}_{\rm in}$), and angular momentum transfer parameter ($m_{\rm AM}$). Note that in the radii where the AGN disk is gravitationally unstable, $\rho_{\rm AGN}$ is proportional to R^{-3}, as the Toomre parameter $Q = \Omega^2/(\sqrt{2}\pi\rho_{\rm AGN})$ becomes 1 (Equation (3) in Thompson et al. 2005), where Ω is the angular velocity of the merger remnant around the supermassive black hole. The $H_{\rm AGN}$ is determined to establish a stable state of the disk following the model of Thompson et al. (2005). On the other hand, to model GW150914-GBM and LVT191012-GBM, we determined $\rho_{\rm AGN}$ and $H_{\rm AGN}$ so that the observed properties of the flares are reproduced. Note that $\rho_{\rm AGN}$ and $H_{\rm AGN}$ are key parameters determining the observed properties, $t_{\rm delay}$, $t_{\rm breakout}$, and $L_{\rm breakout}$.

To estimate the properties of breakout emission from the shock, we assume that the breakout velocity is given by the head velocity of the shocked region, although the directions of the jets may be random (Tagawa et al. 2020a), and the side of the shock (cocoon) may first break out. Since the head velocity is $\sim 5(\theta_{\rm c}/0.2)^{-1}$ times faster than the cocoon expansion velocity (Bromberg et al. 2011), where $\theta_{\rm c}$ is the opening angle of the cocoon, we assume that the cocoon can break out faster than the jet head when the angle between the propagation direction of the jet head and the AGN disk plane is less than $\theta_{\rm c}$. Assuming that the jet direction is random, the probability that the shock breaks out the AGN surface from its head is $\sim \int_0^{\pi/2-\theta_{\rm c}} \sin(\theta) d\theta \Big/ \int_0^{\pi/2} \sin(\theta) d\theta \sim 1 - \theta_{\rm c} \sim 0.8$ for $\theta_{\rm c} = 0.2$. Thus, the shock emission most likely breaks out the AGN disk surface from the head, and we only consider this case.

2.3. Nonthermal Emission

In this subsection, we summarize the properties of the nonthermal emission that emerged after the shock breakout. While photons are trapped in the shock ($\beta_{\rm FS} c > c/\tau$), the shock is mediated by scattering with the photons, in which electrons are not (or inefficiently) accelerated (Ito et al. 2020). Once photons start to escape, a collisionless shock can be formed, where electrons can be accelerated (e.g., Kashiyama et al. 2013; Ito et al. 2020). These electrons produce nonthermal emissions via synchrotron and inverse Compton scattering processes. Here we focus on nonthermal emission after the shock breakout timescale, which is given by $t_{\rm break}$ (Equation (4)) for nonrelativistic and $t_{\rm break,rel}$ (Equation (7)) for relativistic regimes. We focus on the nonthermal emission around the peak of the light curve. The quantitative estimate of the time evolution would require numerical simulations, which is beyond the scope of this paper.

After the breakout of the shock, the nonthermal luminosity decreases depending on the density profile of the AGN disk and the speed of the shock. If the nonthermal radiation emerges—and hence is observed—over a timescale longer than the intrinsic duration of particle acceleration, its brightness will be correspondingly diluted by a factor that we indicate with $f_{\rm dilution}$. For nonrelativistic shocks ($\beta_{\rm FS}\gamma_{\rm FS} \leqslant 1$), we have $f_{\rm dilution} = 1$, since the two timescales are identical. For relativistic shocks in gas pressure–dominated regimes for the AGN disk, since the gas density gradually changes as a function of the distance from the AGN disk plane, the luminosity gradually decreases on the observational timescale; hence, we again assume $f_{\rm dilution} = 1$. On the other hand, for relativistic shocks in radiation pressure–dominated regimes for the AGN disk (which is realized for $R \lesssim 2 \times 10^{-2}$ pc in the fiducial model; e.g., Haiman et al. 2009), the gas density abruptly decreases at a few $H_{\rm AGN}$ (e.g., Grishin et al. 2021). In such cases, the nonthermal luminosity also abruptly decreases and is high only within the timescale of $\sim t_{\rm breakout}$. In this case, the observed emission is diluted on a timescale $t_{\rm dur,NT} = \max(t_{\rm ang}, t_{\rm breakout})$. By assuming for simplicity that the gas density above the AGN disk is almost in a

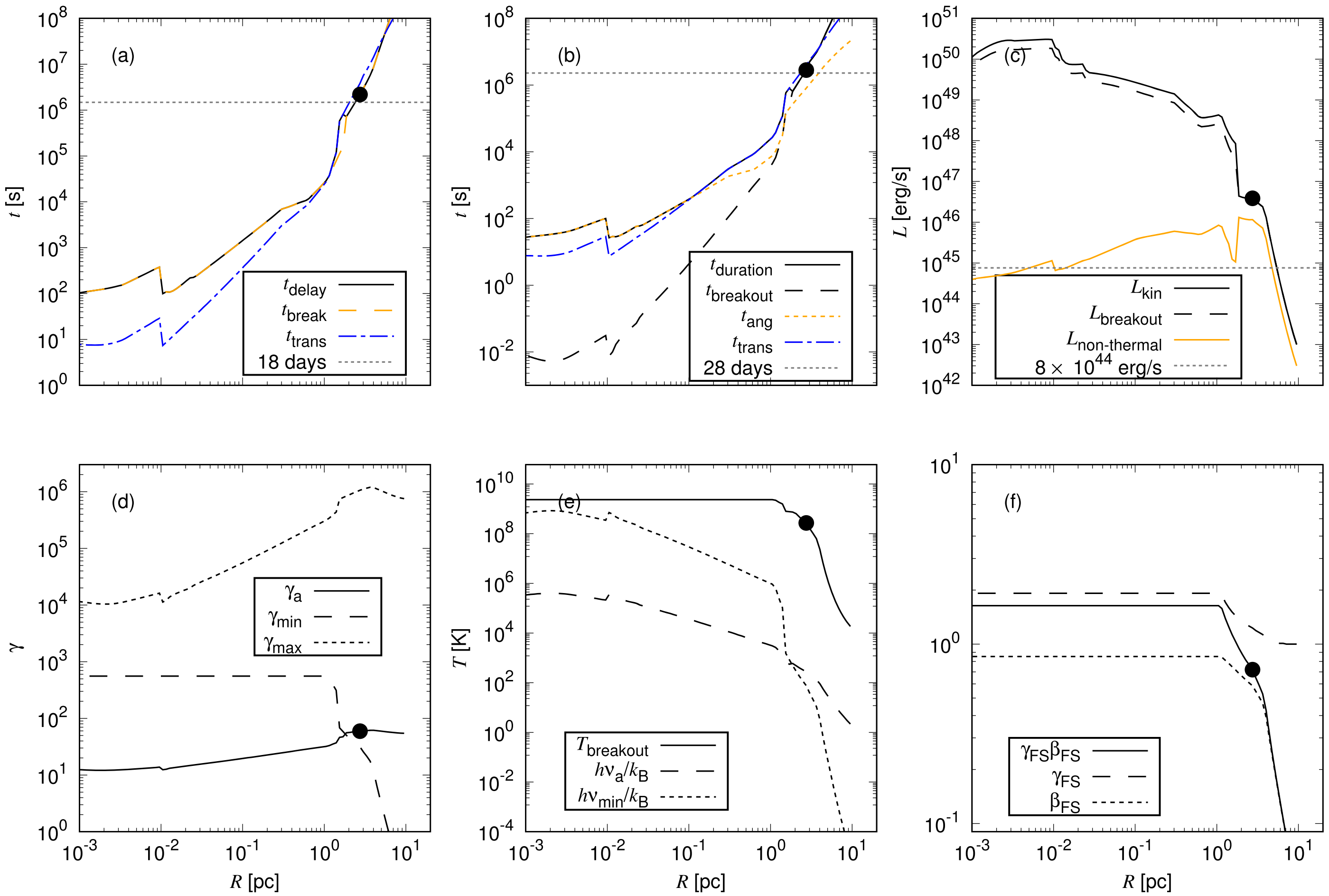

Figure 2. Various quantities as a function of the distance from the supermassive black hole (R) for breakout emission. (a) Timescales representing delay ($t_{\rm delay}$; solid black), breakout ($t_{\rm break}$; dashed orange), and transparency ($t_{\rm trans}$; dashed–dotted blue). (b) Observed duration of the breakout emission ($t_{\rm duration}$; solid black), the duration of the shock breakout ($t_{\rm breakout}$; dashed black), the angular timescale ($t_{\rm ang}$; dotted orange), and the transparent timescale ($t_{\rm trans}$; dotted–dashed blue). (c) Shock (solid black) and breakout luminosity by thermal (dashed black) and nonthermal ($L_{\rm nonthermal}$; orange) emission. (d) Absorption ($\gamma_{\rm a}$; solid) and minimum ($\gamma_{\rm m}$; dashed) and maximum ($\gamma_{\rm max}$; dotted) Lorentz factors. (e) Breakout (solid), absorption ($h\nu_{\rm a}/k_{\rm B}$; dashed), and minimum ($h\nu_{\rm min}/k_{\rm B}$; dotted) temperature. (f) Shock velocity $\gamma_{\rm FS}\beta_{\rm FS}$ (solid), $\gamma_{\rm FS}$ (dashed), and $\beta_{\rm FS}$ (dotted). The black hole locations adopted in the fiducial model are indicated with filled circles superposed on the black solid lines. The dotted horizontal lines in panels (a)–(c) present the observed values for $t_{\rm delay}$, $t_{\rm duration}$, and L at ∼2 eV.

vacuum, we then set $f_{\rm dilution} = t_{\rm breakout}/t_{\rm dur,NT}$ for the cases with relativistic shocks in radiation pressure–dominated regimes. We should note that the assumption may underestimate the nonthermal emission because disk winds might exist that increase the value of $f_{\rm dilution}$.

We assume that a fraction $\epsilon_{\rm e}$ of the kinetic energy of the shock is used to accelerate electrons in a collisionless shock (Sironi et al. 2013). Then, the synchrotron luminosity is given by Fan & Piran (2008),

$$L_{\rm syn} \sim \frac{L_{\rm nonthermal}}{1 + Y_{\rm SSC} + Y_{\rm 2ndIC}} \sim \epsilon_{\rm e} f_{\rm beaming} f_{\rm dilution} \frac{L_{\rm sh}}{1 + Y_{\rm SSC} + Y_{\rm 2ndIC}}, \tag{15}$$

where $Y_{\rm SSC}$ and $Y_{\rm 2ndIC}$ are the powers of synchrotron self-Compton and second-order inverse Compton scattering compared to that of synchrotron emission, and $L_{\rm nonthermal}$ is the luminosity by nonthermal emission. We ignore the inverse Compton scattering of the thermal photons of the AGN disk and those of breakout emission. The former is because its energy density is much lower compared to that of the synchrotron photons. The latter is because the scattering of such photons is typically in the Klein–Nishina regimes in our case. For $\gamma_{\rm sf}\beta_{\rm sf} \leqslant 1$, we set $f_{\rm beaming} = 1$; otherwise, $f_{\rm beaming} = 2\gamma_{\rm sf,f}^2$.

Here the plasma and/or MHD instabilities are assumed to amplify the magnetic field to $\epsilon_{\rm B} \lesssim 10^{-3}$–$10^{-1}$, while electrons are accelerated via the first-order Fermi process with an energy fraction of $\epsilon_{\rm e} \lesssim 10^{-2}$–0.3 (from observations, e.g., Panaitescu & Kumar 2001; Frail et al. 2005; and from theoretical studies, e.g., Spitkovsky 2008; Sironi et al. 2013). We assume that electrons are accelerated in the shock to a power-law distribution of Lorentz factors $\gamma'_{\rm e}$ as $N(\gamma'_{\rm e})d\gamma'_{\rm e} \propto \gamma'^{-p}_{\rm e} d\gamma'_{\rm e}$ with a minimum ($\gamma'_{\rm m}$) and a maximum ($\gamma'_{\rm max}$) value and a power-law index p, where primes are used for quantities in the fluid comoving frame. Assuming that a fraction $\epsilon_{\rm e}$ of the kinetic energy is converted to electron energy, the minimum Lorentz factor $\gamma'_{\rm m}$ is given by

$$\gamma'_{\rm m} \sim \epsilon_{\rm e}\left(\frac{p-2}{p-1}\right)\frac{m_{\rm p}}{m_{\rm e}}(\gamma_{\rm sf} - 1) \sim 40\left(\frac{\epsilon_{\rm e}}{0.3}\right)\left(\frac{\gamma_{\rm sf} - 1}{0.2}\right), \tag{16}$$

where $m_{\rm e}$ is the electron mass.

By comparing the cooling timescale by the synchrotron radiation and the acceleration timescale by the first-order Fermi acceleration mechanism, the maximum Lorentz factor of electrons is determined as

$$\gamma'_{\max} = \frac{v_{\rm sf}}{c}\left(\frac{9\pi e}{10\sigma_{\rm T}B'_{\rm sf}\xi}\right)^{1/2} \\ \sim 1\times 10^{6}\xi^{-1/2}\left(\frac{\beta_{\rm sf}}{0.5}\right)\left(\frac{A_{\gamma_{\rm sf}}}{1.5}\right)^{-1/4} \\ \times\left(\frac{\epsilon_{\rm B}}{0.1}\right)^{-1/4}\left(\frac{\rho_{\rm AGN}}{1\times 10^{-16}\,{\rm g\,cm^{-3}}}\right)^{-1/4}, \tag{17}$$

where e is the electric charge, $A_{\gamma_{\rm sf}} = (\gamma_{\rm sf}-1)(4\gamma_{\rm sf}+3)$,

$$B'_{\rm sf} = (8\pi\epsilon_{\rm B}e'_{\rm sf})^{1/2} \\ \sim 6\times 10^{2}\,{\rm G}\left(\frac{A_{\gamma_{\rm sf}}}{1.5}\right)^{1/2}\left(\frac{\epsilon_{\rm B}}{0.1}\right)^{1/2}\left(\frac{\rho_{\rm AGN}}{1\times 10^{-16}\,{\rm g\,cm^{-3}}}\right)^{1/2} \tag{18}$$

is the magnetic field in the shocked medium (parameterized in terms of the fraction $\epsilon_{\rm B}$ of postshock energy carried by the postshock magnetic field), $e'_{\rm sf} = A_{\gamma_{\rm sf}}\rho_{\rm AGN}c^2$ is the internal energy density of the shocked medium, and ξ is the parameter representing the ratio of the mean free path to the Larmor radius of electrons. We use $\xi = 1$, but this choice only affects $\nu_{\max}$ and has little impact on most of the conclusions in this paper.

The cooling Lorentz factor of electrons, with which electrons can cool in the dynamical timescale due to radiation, is given by

$$\gamma'_{\rm c} = \max\left(1, \frac{6\pi m_{\rm e}c}{\sigma_{\rm T}B'^{2}_{\rm sf}\gamma_{\rm sf}t_{\rm break}}\right), \tag{19}$$

assuming that inverse Compton scattering is subdominant for cooling. Note that nonthermal emission is characterized by fast cooling regimes ($\gamma'_{\rm m} > \gamma'_{\rm c}$) in the fiducial model. The cooling timescale for $\gamma'_{\rm m}$ is

$$t_{\rm c}(\gamma'_{\rm m}) \sim 3\times 10\,{\rm s}\left(\frac{\epsilon_{\rm B}}{0.1}\right)^{-1}\left[\frac{(\gamma_{\rm sf}-1)(4\gamma_{\rm sf}+3)}{1.5}\right]^{-1} \\ \times\left(\frac{\rho_{\rm AGN}}{1\times 10^{-16}\,{\rm g\,cm^{-3}}}\right)^{-1}\left(\frac{\gamma'_{\rm m}}{40}\right)^{-1}\left(\frac{\gamma'_{\rm sf}}{1.2}\right)^{-1}. \tag{20}$$

From $t_{\rm c}(\gamma'_{\rm m})$, the typical shell width of electrons with $\gamma'_{\rm m}$ emitting the synchrotron photons is approximated as $\Delta_{\rm shell}(\gamma'_{\rm m}) \sim t_{\rm c}(\gamma'_{\rm m})v_{\rm FS} \sim 5 \times 10^{11}\,{\rm cm}\ [t_{\rm c}(\gamma'_{\rm m})/30\,{\rm s}]\ (\beta_{\rm FS}/0.5)$.

The Lorentz factor below which synchrotron self-absorption is effective is (Rybicki & Lightman 1979; Fouka & Ouichaoui 2011)

$$\gamma'_{\rm a} = \gamma'_{\rm m}\times(\tau_{\rm q}C_{q+1})^{1/(q+4)}, \tag{21}$$

where

$$\tau_q = \frac{\pi}{3\sqrt{3}}\frac{(q^2+q-2)\gamma_1'^{-5}}{1-(\gamma'_2/\gamma'_1)^{-q+1}} \\ \frac{e\rho'_{\rm sf}\Delta_{\rm shell}(\gamma'_{\rm a})}{B'_{\rm sf}\sin\theta_{\rm PA}m_{\rm p}}, \tag{22}$$

where $\theta_{\rm PA}$ is the typical pitch angle between the magnetic field and the velocity of the electrons, γ_2 and γ_1 are the maximum and minimum Lorentz factors of nonthermal electrons with a power-law index of q around $\gamma_{\rm a}$ while the self-absorption heats electrons, respectively,

$$C_q = \frac{2^{(q+1)/2}}{q+1}\Gamma\left(\frac{q}{4}-\frac{1}{12}\right)\Gamma\left(\frac{q}{4}+\frac{19}{12}\right), \tag{23}$$

where Γ is the gamma function, $C_{p+1}\sim 1.6$ for $q = 2.5$, $n'_{\rm norm}$ is the normalization for the electron number density. We assume that electrons are randomly oriented in the frame of the shocked fluid. We set $\gamma'_2 = \gamma'_{\max}$, $\gamma'_1 = \gamma'_{\rm m}$, and $q = p$ for $\gamma'_{\rm m} < \gamma'_{\rm a}$ and $\gamma'_2 = \gamma'_{\rm m}$, $\gamma'_1 = \gamma'_{\rm a}$, and $q = 2$ for $\gamma'_{\rm a} < \gamma'_{\rm m}$. We determine $\gamma'_{\rm a}$ to satisfy Equations (21) and (22). For $\gamma'_{\rm m} < \gamma'_{\rm a}$, we assume that the power-law slope of the Lorentz factor of electrons during synchrotron self-absorption is the same as the one injected (p) at around $\gamma' = \gamma'_{\rm a}$. If synchrotron self-absorption becomes effective after the synchrotron cooling modifies the electron distribution to the slope of $p-1$, $\gamma'_{\rm a}$ is enhanced by a factor of $\sim$1.08 in the fiducial model (Equation (21)).

With the synchrotron frequency given by

$$\nu_{\rm sync} = \gamma_{\rm sf}\frac{eB'_{\rm sf}}{2\pi m_{\rm e}c} \\ \simeq 2\times 10^{9}\,{\rm Hz}\left(\frac{\gamma_{\rm sf}}{1.2}\right)\left(\frac{B'_{\rm sf}}{600\,{\rm G}}\right), \tag{24}$$

the frequencies corresponding to $\gamma'_{\rm m}$, $\gamma'_{\max}$, and $\gamma'_{\rm a}$ are, respectively (Fan & Piran 2008),

$$\nu_{\rm m} \simeq 3\times 10^{12}\,{\rm Hz}\left(\frac{\gamma'_{\rm m}}{40}\right)^{2}\left(\frac{\nu_{\rm sync}}{2\times 10^{9}\,{\rm Hz}}\right), \tag{25}$$

$$\nu_{\max} \simeq 2\times 10^{21}\,{\rm Hz}\left(\frac{\gamma'_{\max}}{1\times 10^{6}}\right)^{2}\left(\frac{\nu_{\rm sync}}{2\times 10^{9}\,{\rm Hz}}\right) \\ \simeq 2\times 10^{21}\,{\rm Hz}\left(\frac{\xi}{1}\right)^{-1}\left(\frac{\beta_{\rm sf}^{2}\gamma_{\rm sf}}{0.3}\right), \tag{26}$$

and

$$\nu_{\rm a} = 7\times 10^{12}\,{\rm Hz}\left(\frac{\gamma'_{\rm a}}{60}\right)^{2}\left(\frac{\nu_{\rm sync}}{2\times 10^{9}\,{\rm Hz}}\right). \tag{27}$$

For $\nu_{\rm a} < \nu_{\rm m}$, the luminosity by synchrotron radiation is approximately given by Fan & Piran (2008):

$$\nu L(\nu) \sim L_{\rm syn}\times\begin{cases}(\nu/\nu_{\rm m})^{\frac{-p+2}{2}} & \text{for } \nu_{\rm m} < \nu < \nu_{\max}\\ (\nu/\nu_{\rm m})^{1/2} & \text{for } \nu_{\rm a} < \nu < \nu_{\rm m}\\ (\nu/\nu_{\rm a})^{3}(\nu_{\rm a}/\nu_{\rm m})^{1/2} & \text{for } \nu_{\rm syn} < \nu < \nu_{\rm a}.\end{cases} \tag{28}$$

On the other hand, for $\nu_{\rm m} < \nu_{\rm a}$, electrons are thermalized below and around $\gamma_{\rm a}$. We assume that the emission by synchrotron radiation in such cases is approximately given by

$$\nu L(\nu) \sim L_{\rm syn}\times\begin{cases}(\nu/\nu_{\rm m})^{\frac{-p+2}{2}} + \exp(1-(\nu/\nu_{\rm a})^{1/2})\\ \quad \text{for } \nu_{\rm a} < \nu < \nu_{\max}\\ (\nu/\nu_{\rm a})^{3} \quad \text{for } \nu < \nu_{\rm a},\end{cases}$$

where the second term for $\nu_{\rm a} < \nu < \nu_{\max}$ and the luminosity for $\nu < \nu_{\rm a}$ represent emission from thermalized electrons. The order of $\nu_{\rm c} < \nu_{\rm m} < \nu_{\rm a}$ is astrophysically rare (Gao et al. 2013), while it is often realized in the systems we investigated. This is presumably because the ambient material is dense, and the outflow is characterized by its high energy and compact size. The synchrotron self-Compton spectrum of synchrotron photons by thermalized electrons is assumed to be

$$\nu L(\nu) \sim L_{\rm syn} Y_{\rm SSC} \times \begin{cases} \exp(1-(\nu/\nu_{\rm a,SSC})^{1/2}) + (\nu/\nu_{\rm m,SSC})^{(2-p)/2} \\ \quad \text{for } \nu_{\rm a,SSC} < \nu \\ (\nu/\nu_{\rm a,SSC})^2 \\ \quad \text{for } \nu < \nu_{\rm a,SSC}, \end{cases}$$

whose thermal components are derived by considering inverse Compton scattering of synchrotron photons by electrons thermalized by synchrotron self-absorption (with the distribution $N_{\rm e} \propto \gamma^2 \exp(-\gamma/\gamma_{\rm a})$; Ghisellini et al. 1988; Gao et al. 2013), where $\nu_{\rm a,SSC} \approx (4/3)\gamma_{\rm a}'^2 \nu_{\rm a}$ and $\nu_{\rm m,SSC} \approx (4/3)\gamma_{\rm m}'^2 \nu_{\rm m}$ are the absorption and minimum frequencies for synchrotron self-Compton. Note that since the low-energy range of the synchrotron self-Compton spectrum is determined by the upscattered photon distribution, the synchrotron self-Compton spectrum is softer than the synchrotron spectrum. The spectrum of second-order inverse Compton scattering is computed in a similar fashion as that of the synchrotron self-Compton. For $\epsilon_{\rm B} \ll \epsilon_{\rm e}$, $Y_{\rm SSC}$ and $Y_{\rm 2ndIC}$ are approximated as $Y_{\rm SSC} = (\epsilon_{\rm e}/\epsilon_{\rm B})^{1/3}$ and $Y_{\rm 2ndIC} = (\epsilon_{\rm e}/\epsilon_{\rm B})^{2/3}$. Note that second-order inverse Compton scattering is in the Thomson regime if $\max(\nu_{\rm m}\gamma_{\rm m}'^3, \nu_{\rm a}\gamma_{\rm a}'^3) < m_{\rm e}c^2/2$ for the fast cooling regime (Fan & Piran 2008). We do not consider the third-order inverse Compton scattering because it is suppressed by the Klein–Nishina effect, where in the Klein–Nishina regimes, the scattering cross section is reduced compared to Thomson scattering due to quantum electrodynamical corrections (Blumenthal & Gould 1970).

Figure 2 shows the dependence of the properties of emission on the distance R from the supermassive black hole. It can be seen that this dependence is very strong, which can be explained as follows. At smaller radii, the scale height of the disk is lower, and the density of the AGN disk is higher. Due to the higher gas density, the accretion rate onto stellar-mass BHs is higher, resulting in a stronger jet power and higher shock velocity. The delay timescale is also shorter for a smaller-scale height and higher shock velocity (Equation (4)). Also, the duration is shorter for a higher AGN density and shock velocity (Equation (3)). The temperature of the thermal emission is higher for a higher shock velocity and AGN density (Equation (2)). These are the reasons that the properties of emission strongly depend on the radius.

2.4. Numerical Choices

When we discuss the association of ZTF 19abanrhr with GW190521 and predict future electromagnetic counterparts in Section 3, we use the following values for our model parameters. As constrained by Abbott et al. (2020a) and Graham et al. (2020), we assume that the masses of the merged black hole and the supermassive black hole hosting the AGN are $m = 150$ and $M = 10^8\,M_\odot$, respectively. The jet energy conversion efficiency to $\eta_{\rm j} = 0.5$ (Tchekhovskoy et al. 2010), reflecting the spin magnitude of the merged black hole ($a_{\rm BH,rem} \sim 0.7$; Abbott et al. 2020a). In order to reproduce the observed luminosity of the AGN in units of the Eddington luminosity ($L_{\rm Edd}$) to be ∼0.2 (Graham et al. 2020) with a radiation efficiency of $\eta_{\rm rad} = 0.1$, we set the gas inflow rate from the outer boundary ($R_{\rm out} = 10\,{\rm pc}$) of the AGN disk to $\dot{M}_{\rm in} = 50\,L_{\rm Edd}/c^2$, the angular momentum transfer parameter of the AGN disk to $m_{\rm AM} = 0.6$ (Thompson et al. 2005), and the viscous parameter of the AGN disk to $\alpha_{\rm AGN} = 0.1$ (Martin et al. 2019). We assume that the opening angle of the injected jet is $\theta_0 = 0.3$ (Berger 2014; Hada et al. 2018), and the fraction of the accretion rate onto the black hole ($\dot{m}$) over the capture rate to $f_{\rm acc} = 15$ as discussed above. We adopt optimistic values for the fraction of postshock energy carried by the postshock magnetic field and electrons of $\epsilon_{\rm B} = 0.1$ and $\epsilon_{\rm e} = 0.3$ (e.g., Panaitescu & Kumar 2001; Frail et al. 2005; Sironi et al. 2013), respectively, and the power-law slope for injected electrons accelerated by the first-order Fermi process is $p = 2.5$.

3. Results

3.1. Breakout Emission from Merging Black Holes

Breakout emission is expected in association with black hole mergers as follows. The injection direction of the jet is aligned with the black hole spin direction. The black hole spin directions before the mergers tend to be aligned perpendicular to the AGN disk plane. Mergers are generally expected to occur with a different spin direction, since the angular momentum directions of merging binaries are predicted to be quasi-randomized (Samsing et al. 2022) due to frequent binary–single interactions (Tagawa et al. 2020a), in addition to inhomogeneities in the outer regions of the AGN disk (Tagawa et al. 2021b). This results in the reorientation of the jets. Even if the jet eventually aligns with the angular momentum direction of the circum-BH disk due to magnetic interactions, the jet precesses during the alignment process (Liska et al. 2018). Due to the precession, the jet can collide with unshocked gas after merger. The other possibility is that gas accretes onto the remnant with the angular momentum direction modified due to the shocks formed by recoil kicks caused by gravitational wave radiation. Then, the jet can propagate in the modified direction. In all of the above cases, after this reorientation, as the jet once again collides with unshocked gas, shocks emerge, and breakout emission is released following the emission of gravitational waves (Figure 1(b)). We predict the properties and detectability of the breakout emission in this model applied to possible electromagnetic counterparts of gravitational-wave events.

Figure 3 shows the SED for emission from typical merging black holes ($m = 60\,M_\odot$ and $d_{\rm L} = 500\,{\rm Mpc}$) at $R = 1\,{\rm pc}$ with $f_{\rm acc} = 15$ (panel (a)) and $R = 10^{-2}\,{\rm pc}$ with $f_{\rm acc} = 1$ (panel (b)). The dotted orange line shows the sensitivity for the Fermi GBM. The integration time is limited by $t_{\rm duration}$ presented in the legend, while $t_{\rm int} = 10^4\,{\rm s}$ is adopted for the sensitivities of Swift BAT in (panel(a)).

3.2. Properties of Breakout Emission

We first predict the characteristic properties of the breakout emission from a merging black hole. To understand the detectability of the breakout emission from common black hole mergers, Figure 3 shows the parameter dependence of the spectral energy distribution (SED) of the breakout emission adopting $m = 60\,M_\odot$, $d_{\rm L} = 500\,{\rm Mpc}$, and $R = 1\,{\rm pc}$ (panel (a)) and $R = 10^{-2}\,{\rm pc}$ (panel (b)). We assume $f_{\rm acc} = 15$ for $R = 1\,{\rm pc}$ and $f_{\rm acc} = 1$ for $R = 10^{-2}\,{\rm pc}$, since the accretion rate can be enhanced by the recoil kick if the delay timescale is long enough that shocked gas can accrete onto a black hole before the breakout (Appendix B). For mergers at $R = 1$ pc, nonthermal emission can be discovered by ZTF, the Vera Rubin Observatory, the Roman Space Telescope, HiZ-GUNDAM, and the Einstein Probe and can also be detected by follow-up observations by Chandra, XMM-Newton, the Nuclear Spectroscopic Telescope Array (NuSTAR), Focusing On Relativistic universe and Cosmic Evolution (FORCE), the Wide-field Infrared Survey Explorer (WISE), and the James Webb Space Telescope (JWST) once the source direction is localized by ZTF. Additionally, thermal emission from $R = 1$ and 10^{-2} pc can be detected by the Swift Burst Alert Telescope (BAT). However, for $R = 10^{-2}$ pc, the detection probability is reduced by the beaming effect by a factor of $\sim 1/\gamma_{\rm sf,f}^2 \sim 1/16$ compared to cases with $\gamma_{\rm sf,f} \sim 1$, since the opening angle of the jet at a breakout of $\theta_j \sim 0.08 (<\theta_0)$ (Bromberg et al. 2011) is smaller than $1/\gamma_{\rm sf,f}$, where $\gamma_{\rm sf,f}$ is the final Lorentz factor of the shocked gas. In addition, Swift BAT needs to direct to the source beforehand, since there is not enough time for the telescope to redirect due to the short delay time ($\sim 10^2$ s) and duration (~ 30 s), which further reduces the observational probability by a factor of ~ 10. Thus, for mergers in $R \gtrsim$ pc, optical surveys and/or future X-ray monitors can detect electromagnetic counterparts, as suggested for ZTF 19abanrhr; then, infrared and X-ray pointing facilities can detect it later. For $R \lesssim 10^{-2}$ pc, electromagnetic counterparts are difficult to discover unless they are bright enough to be detected by the Fermi GBM and/or the anticoincidence shield of the spectrometer on board INTEGRAL (SPI-ACS), as suggested for GW150914-GBM and LVT151012-GBM.

In Figure 3(a), the luminosity from the host AGN in the relevant energy range is given by

$$\nu L_{\rm AGN}(\nu) \sim 10^{44}\ {\rm erg\ s^{-1}} \\ (M/10^8\,M_\odot)(\dot{M}c^2/L_{\rm Edd})(f_{\rm cor}/10)^{-1}, \tag{29}$$

where $f_{\rm cor}$ is the correction fraction from the total luminosity to the luminosity at some frequency. As depicted by the solid blue lines in Figures 3 and 4, we assume that $f_{\rm cor} \sim 5$ at $c/\nu = 4400$ Å and extrapolate the luminosity for $10^{12}\ {\rm Hz} \lesssim \nu \lesssim 10^{15}$ Hz using the cyan or blue points in Figure 7 of Ho (2008), depending on the assumed Eddington ratio, and $f_{\rm cor} \sim 10$ in $0.1\ {\rm keV} \leqslant h\nu$ (Ho 2008; Trakhtenbrot et al. 2017; Duras et al. 2020) with the upper exponential cut off at 300 keV (Ricci et al. 2018). We also assume that the fraction of the variable luminosity compared to the average luminosity in optical bands with $t_{\rm duration} \lesssim 0.1$ yr is $f_{\rm var} \lesssim 0.1$ (Kozłowski 2016), and that in X-ray bands is $f_{\rm var} \sim 0.3$ (Soldi et al. 2014; Maughan & Reiprich 2019, dashed blue lines).

3.3. ZTF 19abanrhr and GW190521

3.3.1. Observed Properties

We overview the observed properties for ZTF 19abanrhr. Graham et al. (2020) reported that the optical transient ZTF 19abanrhr from AGN J124942.3+344929 at $z = 0.438$ is possibly associated with GW190521. The optical flare in ZTF 19abanrhr began to exceed the persistent flux from the AGN activity after ~ 18 days (in the rest frame) from the occurrence of the merger event, GW190521. The peak luminosity of ZTF 19abanrhr is $\sim 8 \times 10^{44}\ {\rm erg\ s^{-1}}$ in the g and r bands with an observed duration of ~ 28 days (in the rest frame). Before and after the peak, the luminosity increases and decreases roughly exponentially. The change in the slope of the luminosity is somewhat shallower in the latter. The color is consistent with a constant with $g - r \sim 0.2$, while it appears to be reduced to $g - r \sim 0.15$ during the flare. The mass of the supermassive black hole hosting AGN J124942.3+344929 is $M \sim 10^8$–$10^9\,M_\odot$, and the luminosity of the AGN in units of the Eddington luminosity is ~ 0.02–0.2 (Graham et al. 2020). The mass of the merged remnant is $m \sim 150\,M_\odot$, and its dimensionless spin is $a_{\rm BH,rem} \sim 0.7$ (Abbott et al. 2020a). The inclination angle (the angle between the total angular momentum of the merged binary with respect to the line of sight) is estimated to be $\sim 40°$–$60°$ (Abbott et al. 2020a; Calderón Bustillo et al. 2021), disfavoring a transient with high luminosity due to a significant beaming of emission from the Blandford–Znajek jet or its shock, since the spin of a merged remnant and, accordingly the Blandford–Znajek jet are expected to be aligned with the total angular momentum of the merged binary. Note that the inclination angle estimated by Gayathri et al. (2022) is different from that above. Thus, the possible beaming of emission associated with gravitational-wave events may be useful to constrain the parameters of black hole mergers observed by gravitational waves.

The association significance of ZTF 19abanrhr to GW190521 is under debate (Ashton et al. 2021; Calderón Bustillo et al. 2021; Palmese et al. 2021). Ashton et al. (2021) analyzed that the chance occurrence probability of the association of GW190521 and ZTF 19abanrhr is between $\sim 8\%$ and 50%. Palmese et al. (2021) estimated that the chance occurrence probability is $\sim 4\%$ and $\sim 70\%$ by using a damped random walk model adopted in Graham et al. (2020) and a more general structure function, respectively. Here a damped random walk model well describes the structures of flares from AGN disks for the duration of flares to be less than ~ 1 yr (Kozłowski 2016). Calderón Bustillo et al. (2021) found that with different priors (uniform in inverse of a mass ratio, 1–4, instead of uniform in a mass ratio, 1/4–1), the chance occurrence probability is reduced to $\sim 1\%$ due to the modification for the position of GW190521 in different preferences for the mass ratio. Currently, the association is considered to be tentative. There are also several independent suggestions that GW190521 originated in an AGN disk (Yang et al. 2020; Tagawa et al. 2021a), especially if the suggested high eccentricity is true (Romero-Shaw et al. 2020; Tagawa et al. 2021b; Gayathri et al. 2022; Samsing et al. 2022).

3.3.2. Model for ZTF 19abanrhr

Here we discuss whether the possible association of ZTF 19abanrhr with GW190521 can be explained by emission from black holes merging in an AGN disk. We focus on this association here but note that other optical associations were reported (Graham et al. 2023) as the present manuscript was being prepared for submission. The properties of the additional flares are similar to those of ZTF 19abanrhr and broadly consistent with our model. The fits in our model to these flares require a range of different parameter choices and will be presented in a follow-up paper. We adopt parameter values to match the observed properties of this source (Section 2.4). To propose a consistent model for this association, it is crucial to simultaneously explain (I) all of the several observed properties of the flare and (II) the reason why there is no bright emission before the merger.

(I) Several properties of the flare are obtained by the ZTF observations, which include its luminosity in the optical bands, its color, and its time evolution (Section 3.3.1). Figure 4 shows the properties of thermal and nonthermal emission at the shock breakout of a jet produced from merging black holes. The discontinuities at distances from the central supermassive black hole of $R \sim 1$ and ~ 0.01 pc are, respectively, due to the transition from subrelativistic to relativistic regimes and to gap formation around black holes by their gravitational torques caused by the transition for the opacity of AGN disk gas. In this model, the delay timescale ($t_{\rm delay} \sim 19$ days; Figure 4(a)) and the observed duration of the breakout emission for nonthermal photons ($t_{\rm duration} \sim 23$ days; panel (a)) are, respectively, comparable to the observed delay time and the duration (dotted gray lines), provided the merger occurs at $R \sim 2.5$ pc. In the breakout emission, the delay timescale is calculated by the time for the shock to reach the edge of the AGN disk (Equation (4)), while the duration is calculated by the time that photons diffuse out from a breakout shell to the edge of the AGN disk (Equation (3); see Section 2.2). Since the observable properties, especially the timescales, are mostly influenced by R (Figure 4), flares similar to the previous one (ZTF 19abanrhr if it was real) are expected to be observed in the future if there is a hot spot for the merging location (Section 4). Figure 5 shows the SED of the emission at $R = 2.5$ pc. The luminosity at $\sim 6 \times 10^{14}$ Hz, arising from synchrotron emission from the nonthermal electrons accelerated at the forward shock, is roughly consistent with the observed value of $\nu L_\nu \sim 8 \times 10^{44}$ erg s^{-1}. The power-law spectral slope (s, $\nu L_\nu \propto \nu^s$) of the synchrotron emission is given by $s = -0.25$, while the observed slope during the flare corresponding to the color $g - r = 0.15$–0.2 is $s = -(0.45$–$0.6)$ (Graham et al. 2020). Since the contribution of the flare to the background AGN luminosity is $\sim$30% and the slope of the background emission is $s \sim -0.6$ ($g - r = 0.2$), the slope for the combination of the flare and the background emission is estimated to be ~ -0.5 at the observed wavelengths of 470 and $\sim$650 nm. Hence, the synchrotron emission is roughly consistent with the observed color during the flare. The remarkable point of the estimates is that the delay time, duration, and luminosity of ZTF 19abanrhr are well reproduced for the same value of the location within the disk, that is, $R = 2.5$ pc (Figure 4), although the luminosity is somewhat adjusted (Section 2.4). For the nonthermal emission, the peak of the light curve likely comes when the forward shock reaches the edge of the AGN disk (Perna et al. 2021a). A more quantitative estimate of the light curves for the nonthermal emission will require numerical simulations, which is beyond the scope of this paper (see Section 2.3).

(II) Another issue, which needs to be resolved to claim the association, is that intense emission should be launched only after the merger of GW190521. In the models for emission from the shock around the jet, this requires (a) the existence of cold gas in the direction of the jet propagation from the merger remnant and (b) gas accretion within the delay between GW190521 and ZTF 19abanrhr. The fact that the emission is produced only after the merger has not been addressed or fully explained in previous models for the association. Recoil kicks might offer a solution. Graham et al. (2020) proposed that the merger remnant moves to unperturbed dense gas as a result of the recoil kick and begins to accrete. However, it is unclear why circumbinary gas should not already be present and power bright emission prior to the merger (Farris et al. 2015; Tang et al. 2018). One possibility is that a cavity preexists around the remnant, carved out by radiative and/or mechanical feedback from the merging black holes; the merger remnant then moves to unshocked regions at the boundary of this cavity by recoil kicks (Kimura et al. 2021). On the other hand, with the parameters ($R \gtrsim$ pc) constrained above, it takes too long ($\gtrsim$yr) to reach replenished gas, compared to the $\sim$month delay between GW190521 and ZTF 19abanrhr (Section 4.1). As discussed above, the model for breakout emission can explain why bright emission is observed only after the mergers (Figure 1(b)). We conclude that breakout emission from shocks driven by a Blandford–Znajek jet can explain the properties of the transient, ZTF 19abanrhr, possibly associated with GW190521.

We further predict how the breakout emission similar to ZTF 19abanrhr can be observed by various telescopes in the future. We employ parameters to explain ZTF 19abanrhr as a fiducial model (see Section 2.4). Figure 5 shows the SED for the breakout emission assuming a luminosity distance $d_{\rm L} \sim 3$ Gpc to the event together with the sensitivity curves of various equipment. Nonthermal emission can be detected by ZTF, the Vera Rubin Observatory, and the Roman Space Telescope (solid black, dotted cyan, and dotted green lines in Figure 5; see Appendix C for their properties). Thermal emission can be detected by future wide-field X-ray surveys HiZ-GUNDAM and the Einstein Probe if breakout emission is produced closer to us (e.g., $d_{\rm L} \lesssim$ Gpc). Chandra, XMM-Newton, NuSTAR, FORCE (a future hard X-ray telescope), WISE, and JWST can detect emission from such merger remnants if the merger event is well localized by other observations, since the time spent for directing to the source ($\sim$day) is shorter than the duration of the emission for mergers at $R \gtrsim$ pc ($\sim$0.1 yr; Figure 4(b)). Since the timing and duration of the emission is the same at all wavelengths, from infrared to gamma rays, the emission can be simultaneously observed in a wide range of wavelengths with bright optical emission. We propose that such follow-up observations in infrared and X-ray bands can be a smoking-gun signature of this scenario, leading to a first confirmation of the origin of the black hole mergers. Then, we can further derive the properties of the mergers' environments as described for several possible associations above and in Section 2.

3.4. GW150914-GBM and LVT151012-GBM

3.4.1. Observed Properties

We next describe the observed properties of GW150914-GBM. Associated with GW150914, the Fermi GBM might have detected a transient of luminosity $\sim 2 \times 10^{49}$ erg s^{-1} at energies of $\sim$10 keV–several MeV with spectral shape $\nu L_\nu \propto \nu^{p_{\rm s}}$ with $p_{\rm s} \sim 0.6$. The possible transient was observed $\sim$0.4 s after the gravitational-wave event with a duration of $\sim$1 s. The signal-to-noise ratio was estimated to be 5.1 with a false-alarm probability for the association with GW150914 of 0.0022 (2.9σ; Connaughton et al. 2016). Several criticisms and/or issues were raised by a number of studies (Greiner et al. 2016; Savchenko et al. 2016), and they are answered or discussed in Connaughton et al. (2018). A possible problematic point is that INTEGRAL SPI-ACS put constraints on the gamma-ray intensities at 75 keV–2 MeV in the direction of GW150914 at the merger (Savchenko et al. 2016). On the other hand, since INTEGRAL is most sensitive at $\sim$100 keV (Figure 3 in Savchenko et al. 2016), while the peak energy inferred for GW150914-GBM is $\sim 3.5^{+2.1}_{-1.1}$ MeV, and the estimated spectral index is hard, it can be barely consistent with the nondetection by INTEGRAL SPI-ACS (Connaughton et al. 2018; see Figure 3(b)). Connaughton et al. (2018) discussed that a weaker signal estimated by the analyses in Greiner et al. (2016) may be preferred for consistency with the nondetection by INTEGRAL SPI-ACS.

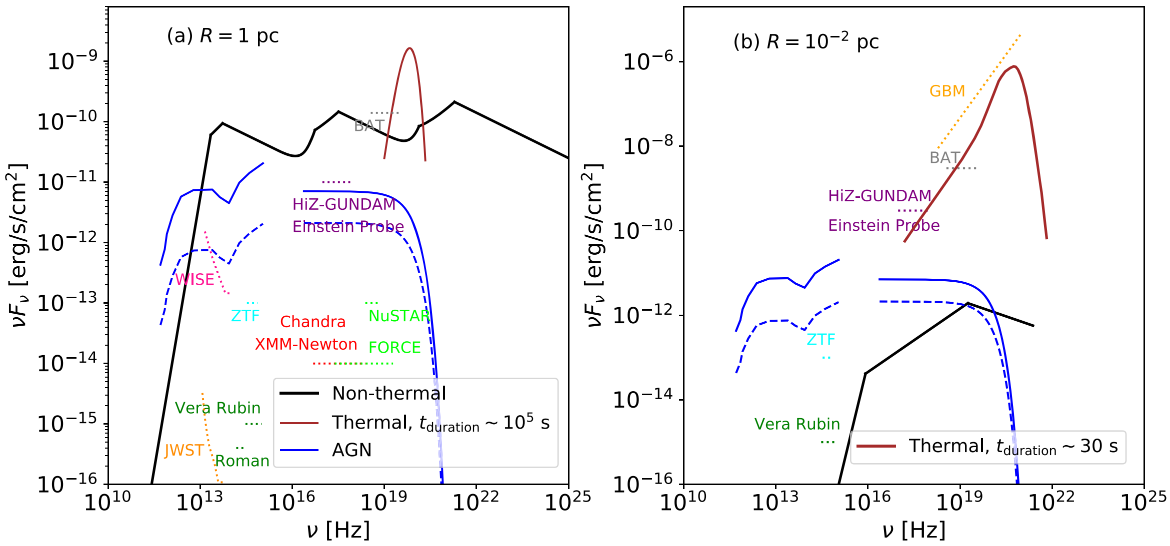

Figure 3. The SED for nonthermal (solid black) and thermal (solid brown) emission from typical merging black holes in AGN disks ($m = 60\,M_\odot$ and $d_{\rm L} = 500$ Mpc) at $R = 1$ pc with $f_{\rm acc} = 15$ (panel (a)) and $R = 10^{-2}$ pc with $f_{\rm acc} = 1$ (panel (b)). Solid and dashed blue lines represent emission from the host AGN and its variability amplitude, respectively. The dotted cyan, dark green, gray, purple, red, light green, pink, and orange lines mark the sensitivity of ZTF, the Vera Rubin Observatory and Roman Space Telescope, Swift BAT, HiZ-GUNDAM and Einstein Probe, Chandra and XMM-Newton, NuSTAR and FORCE, WISE, and JWST, respectively. The integration time for observations is set to the $t_{\rm duration}$ presented in the legend, while $t_{\rm int} = 10^4$ s is adopted for the sensitivities of Swift BAT in panel (a).

Additionally, Bagoly et al. (2016) reported another possible electromagnetic association with the gravitational-wave event, LVT151012, with a false-alarm probability of 0.037. Event LVT151012 is a tentative gravitational-wave event for the merger of 23^{+18}_{-5} and $13^{+4}_{-5}\,M_\odot$ at $d_L = 1100^{+500}_{-500}$ Mpc with a false-alarm rate of 0.44 yr^{-1} and a false-alarm probability of 0.02 (Abbott et al. 2016b). The burst looks similar to GW150914-GBM. It has a similar flux, it occurred within seconds of the gravitational-wave event with a duration of seconds, and the peak energy is found to be between 130 keV and 3.5 MeV.

Although, unlike for GW190521, the inclination angle (the angle between the total angular momentum of the merged binary with respect to the line of sight) for GW150914 and LVT151012 was not significantly constrained due to the lack of detection of the higher-order multipole modes (Abbott et al. 2016c), constraints on the inclination angle in future gravitational-wave observations associated with gamma-ray counterparts would be very useful, since low values of the inclination angle are required to explain the association of GW150914-GBM by our model, as discussed in the next section.

3.4.2. Model for GBM Events

We also find that the properties, including the luminosity, delay time, duration, and color, of the transients suggested to be associated with GW150914 and LVT151012 can be explained by thermal emission from black hole mergers at $R = 10^{-4}$ and $\lesssim 10^{-4}$ pc, respectively.

A model for this candidate source needs to explain the observed hard spectrum (red circles in Figure 5(b)). A possible process reproducing the spectrum is thermal emission. The peak energy of the transient is about $\sim$3 MeV, while annihilation of gamma rays prohibits strong thermal emission above $\sim$1 MeV in the rest frame (Budnik et al. 2010; Ito et al. 2020). To explain the strong emission at $\sim$3 MeV, the observer needs to be within the beaming direction of the shock at breakout with a Doppler shift by a factor of $\sim$4–10 (Figure 5(b)). The spectral shape of the thermal

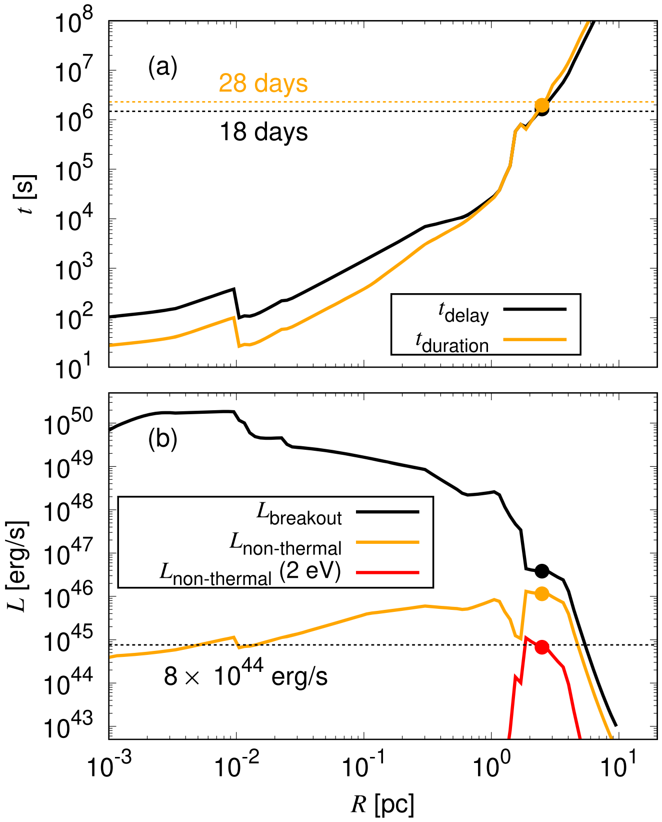

Figure 4. Timescales and luminosities of shock breakout emission produced around merging black holes as a function of the distance from the supermassive black hole (R). (a) Delay timescale ($t_{\rm delay}$; black) and observed duration of breakout emission ($t_{\rm duration}$; orange). (b) Breakout luminosity of the thermal ($L_{\rm breakout}$; black) and nonthermal emission at its peak frequency ($L_{\rm nonthermal}$; orange) and at $h\nu = 2$ eV ($L_{\rm nonthermal}$(2 eV); red), including Doppler beaming. The black hole locations adopted in the fiducial model are indicated with filled circles superposed on the lines. The dashed horizontal lines present the observed values for $t_{\rm delay}$, $t_{\rm duration}$, and L at $\sim$2 eV.

emission in Figure 5(b) is adopted from that calculated by Ito et al. (2020) considering $\gamma\gamma$ annihilation. For these events, we assume the Bondi–Hoyle–Lyttleton rate for the accretion rate onto the merged remnant (Section 2.1).

We constrain the model parameters as follows. First, to produce the spectral peak energy, we adopt $\gamma_{\rm sf,f} \sim 5$, reflecting the discussion above. The observed delay timescale of $t_{\rm delay} \sim 0.4$ s and $\gamma_{\rm sf,f} \sim 5$ together can be used to constrain the scale height of the AGN disk to $H_{\rm AGN} \sim 3 \times 10^{11}\,{\rm cm}(\gamma_{\rm sf,f}/5)^2(t_{\rm delay}/0.4\ {\rm s})$ (see Equation (7)). The observed breakout luminosity ($L_{\rm breakout}$) is proportional to the jet power ($L_{\rm j}$) and the accretion rate onto the black hole $\dot{m}$ (Equation (1)), which is adjusted by changing the AGN density at the location of the black hole ($\rho_{\rm AGN}$) and the supermassive black hole mass (M) given the mass of the merged remnant (m), R, and $\gamma_{\rm sf,f}$ (Tagawa et al. 2022). Additionally, the initial opening angle of the jet θ_0 at launch can be determined to reproduce $\gamma_{\rm sf,f}$ with a given $H_{\rm AGN}$, $\rho_{\rm AGN}$, and $L_{\rm j}$ (Bromberg et al. 2011). By adopting $\rho_{\rm AGN} = 4 \times 10^{-6}\,{\rm g\,cm^{-3}}$, $M = 10^6\,M_\odot$, $R = 10^{-4}$ pc, and $\gamma_{\rm sf,f} = 5$, we can derive $\theta_0 = 0.06$, $H_{\rm AGN} \sim 3 \times 10^{11}$, $L_{\rm j} = 10^{48}\,{\rm erg\,s^{-1}}$, $L_{\rm breakout} = 1.5 \times 10^{49}\,{\rm erg\,s^{-1}}$ (including Doppler beaming), the delay time $t_{\rm delay} = 0.4$ s (using Equation (7)), and the duration $t_{\rm duration} = 0.2$ s (using Equation (11)). Note that $t_{\rm duration} = 0.2$ s is shorter than the inferred total duration of $\sim$1.0 s. On the other hand, the duration of the phase with the above bright luminosity is $\lesssim 1/4$ s (Figure 7 in Connaughton et al. 2016), consistent with the value derived here (see also Bagoly et al. 2016). The light curve is expected to grow superexponentially at breakout (Sapir et al. 2011), and after breakout emission, the luminosity decays as a power law in time (Nakar & Sari 2012). The inferred density ($\rho_{\rm AGN} = 4 \times 10^{-6}\,{\rm g\,cm^{-3}}$) together with $R = 10^{-4}$ pc, $H_{\rm AGN} \sim 3 \times 10^{11}$, and $M = 10^6\,M_\odot$ is realized for an AGN disk with a common accretion rate of $\dot{M} \sim 0.2\,L_{\rm Edd}/c^2$ and a viscous parameter of $\alpha_{\rm AGN} = 0.1$. Thus, even without identifying a host AGN, if our model correctly predicts the electromagnetic emission, we can derive the properties of the AGN, such as $H_{\rm AGN}$, $\rho_{\rm AGN}$, and R, where black hole mergers often occur. The SED adjusted to explain GW150914-GBM is presented in Figure 5(b).

Although we consider the collision of the jet with the inner regions of the AGN disk, it may also be possible to produce similar emission by considering the collision of the jet with a circum–black hole disk, whose size is $\sim 3 \times 10^{11}$ cm for the mass of the merged remnant of $m \sim 60\,M_\odot$, and the accretion rate onto the black hole of $\dot{m} \sim 10^4\,l_{\rm Edd}/c^2$ assuming a slim disk model (Abramowicz et al. 1988).

The properties of the transient possibly associated with LVT151012 (Section 3.4.1) can also be explained by a similar parameter set, while the higher luminosity (due to the larger distance by a factor of $\sim$2) and the lower peak energy (roughly around MeV) require a higher $\rho_{\rm AGN}$ and lower $\gamma_{\rm sf,f}$. These can be explained by a merger at smaller R, where $\rho_{\rm AGN}$ is higher and a lower $\gamma_{\rm sf,f}$ is preferred to reproduce the delay time ($\sim$1 s) due to a smaller $H_{\rm AGN}$.

In summary, in the model of emission from merging black holes in an AGN disk, there exists a set of parameters for which the properties of ZTF 19abanrhr, GW150914-GBM, and LVT151012-GBM can be explained.

4. Discussions

In this section, we discuss the probability of observing breakout emission from merging black holes, the possible obscuration by a dust torus, the parameter dependence of the results, and the merging location within the AGN disk. Specifications of several telescopes that might be able to detect the breakout emission at different wavelengths are summarized in Appendix C.

4.1. Probability of Observing Breakout Emission from Merging Black Holes

We suggest that breakout emission from merging black holes may be easier to discover compared to that from solitary black holes for the following reasons. (A) By using gravitational-wave observations, constraints on the spatial localization and the timing of flares are modestly and significantly improved, respectively, thus removing the need to continuously monitor large sky areas to search for rare flares. (B) The accretion rates onto merger remnants may be enhanced due to recoil kicks (see below). (C) The spin magnitudes of black holes are enhanced to $a_{\rm BH,rem} \sim 0.7$ by the merger (Buonanno et al. 2008), increasing the jet luminosity. Although the spin magnitudes of solitary black holes ($a_{\rm BH,iso}$) are highly uncertain, spin-up by accretion and spin-down by the Blandford–Znajek jet may be roughly equal at around $a_{\rm BH,iso} \lesssim 0.3$ (e.g., Figure 10 of Narayan et al. 2022). Assuming $a_{\rm BH,iso} \sim 0.3$, the jet luminosity is enhanced by a factor of $\sim(a_{\rm BH,rem}/a_{\rm BH,iso})^2 \sim 5(a_{\rm BH,rem}/0.7)^2(a_{\rm BH,iso}/0.3)^{-2}$. (D) The merging black holes may be more massive than isolated black holes as inferred from gravitational-wave observations (The LIGO Scientific Collaboration et al. 2021), producing brighter emission due to higher accretion rates.

In order for emission to be produced shortly after mergers (roughly within a timescale comparable to the duration of the flare) and discovered using gravitational-wave observations, several key elements are needed. First, gas needs to be present along the direction of propagation of the jet (black hole spin) of the merged remnant; otherwise, thermal and nonthermal emission from dissipation of the jet power would not be expected. The shape of the ejected region is cylindrical with an aspect ratio of $\sim\theta_0 f_{\rm ext} \sim 1(\theta_0/0.3)(f_{\rm ext}/3)$ (Tagawa et al. 2022), where θ_0 is the opening angle of the injected jet, $f_{\rm ext}$ is the fraction of the radial extent of the shocked regions advanced after the breakout from the AGN disk over that at the breakout, and $f_{\rm ext} \sim 3$ is motivated for a spherical explosion in a background with an exponential gas density profile (Olano 2009). Hence, gas presumably exists at the merger, except in the cylindrical regions that have been ejected before the merger in previous episodes of jets launched from the progenitor black holes. Since the angular momentum directions of binaries are predicted to be random at mergers in AGN disks due to frequent binary–single interactions (Tagawa et al. 2020a; Samsing et al. 2022) and inhomogeneities in the outer regions of the AGN disk, the directions of the spins of the merged remnants and that of the jet propagation are plausibly randomized at mergers. Thus, gas often exists in the direction of the spin of the merged remnants (Figure 1(b)), with a probability of $P_{\rm col} \sim \cos({\rm atan}(\theta_0 f_{\rm ext})) \sim 0.7$ for $\theta_0 \sim 0.3$ and $f_{\rm ext} \sim 3$. If we assume $\theta_0 \sim 0.03$–0.5 (Berger 2014; Hada et al. 2018) and $f_{\rm ext} \sim 1$–5 (Olano 2009), $P_{\rm col}$ ranges in the interval of $\sim$0.4–1.

The second issue is that gas needs to be accreted onto the merged remnant for a flare to occur in association with a black hole binary merger. Here we assume that the flare can be considered to be associated with a gravitational-wave event when the delay timescale is roughly comparable to or less than the duration of the flare, since it is probably difficult to find an association with a short duration and long delay time. Kimura et al. (2021) proposed that electromagnetic counterparts may be

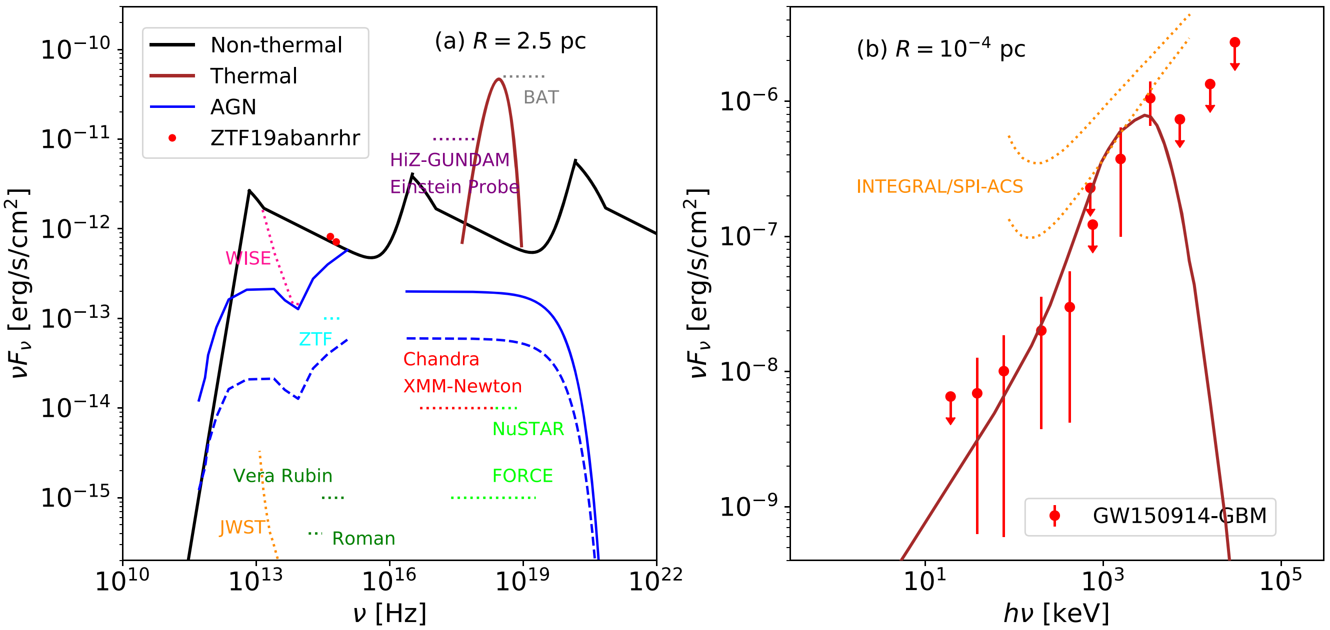

Figure 5. Same as Figure 3, but the results are specific for emission concerning the putative associations with gravitational-wave events. We show the SED for $R = 2.5$ (panel (a)) and 10^{-4} (panel (b)) pc. The dotted cyan, dark green, gray, purple, red, light green, pink, and orange lines mark the sensitivity of ZTF, the Vera Rubin Observatory and Roman Space Telescope, Swift BAT (with an integration time of $t_{\rm int} = 10^5$ s), HiZ-GUNDAM ($t_{\rm int} = 10^4$ s) and Einstein Probe ($t_{\rm int} = 10^3$ s), Chandra ($t_{\rm int} = 2 \times 10^4$ s) and XMM-Newton ($t_{\rm int} = 10^4$ s), NuSTAR ($t_{\rm int} = 10^6$ s) and FORCE ($t_{\rm int} = 10^6$ s), WISE ($t_{\rm int} = 10^4$ s), and JWST ($t_{\rm int} = 10^4$ s), respectively. The red points in panel (a) correspond to the observed luminosity of ZTF 19abanrhr in the r and g bands assuming $g - r \sim 0.15$, and those in panel (b) represent the observed luminosity of GW150914-GBM with 1σ error bars. The dotted orange curves mark the range of sensitivity of INTEGRAL SPI-ACS assuming $d_{\rm L} = 410$ Mpc (Savchenko et al. 2016). For thermal emission in panel (b), we use the spectral shape given as the purple line in Figure 4 in Ito et al. (2020) boosted to a higher energy by $\gamma_{\rm sf,f} = 5$.

produced by moving to unshocked regions by the gravitational-wave recoil kick after merger. Usually, gas replenishment by the recoil kick takes a longer time compared to $t_{\rm delay}$ and $t_{\rm duration}$. The kick velocity due to gravitational-wave radiation ($v_{\rm rk}$) is on the order of $\sim 10^2$–$10^3\,{\rm km\,s^{-1}}$, and the gas is depleted within $r_{\rm dep} \sim f_{\rm ext} H_{\rm AGN} \theta_0 \sim 10^{16}\,{\rm cm}(R/{\rm pc})$ (Tagawa et al. 2022), where $H_{\rm AGN}$ is the scale height of the AGN disk at R. Then, the kicked black hole crosses the cavity on a timescale of

$$t_{\rm arr} \sim r_{\rm dep}/v_{\rm rk} \sim 30\,{\rm yr}\,(v_{\rm rk}/3 \times 10^2\,{\rm km\,s^{-1}})^{-1}(R/3\,{\rm pc}). \quad (30)$$

Such a long delay time ($t_{\rm arr}$) compared to the short duration (orange line in Figure 2(a)) would not be regarded as association in observations. In ZTF 19abanrhr, the observed delay time of ~ 0.05 yr is much shorter than the arrival timescale in Equation (30). To expect a flare with a short delay whose timescale is comparable to the observed delay time, the merging black holes need to have circum–black hole disks at the merger. Adopting the model in Tagawa et al. (2022), we derive that $P_{\rm active} \sim 0.03$ at $R \sim 3$ pc, where $P_{\rm active}$ is the probability that a merged remnant accompanies a circum–black hole disk and a jet, although the active probability strongly depends on the model parameters. On the other hand, if mergers are significantly facilitated by circum–black hole disks, which is not assumed in the discussions above, merged remnants may tend to accompany circum–black hole disks (Farris et al. 2015; Tang et al. 2018). Bartos et al. (2017) assessed mergers to be significantly facilitated by circum–black hole disks, while Tagawa et al. (2020b) found the opposite by applying the updated theory of gap formation (Duffell et al. 2014). Note that both studies assumed that the accretion onto black holes is limited at around the Eddington rate, which may underestimate the effect on binary evolution by circum–black hole disks because the disk mass can be much higher for highly super-Eddington accretion disks; hence, the influence of torques from circum–black hole disks on mergers has not been quantitatively understood. Since $P_{\rm active}$ is estimated to be larger than ~ 0.01 (Tagawa et al. 2022), and significant facilitation of mergers by circumbinary disks may enhance $P_{\rm active}$ up to 1, we assume as a rough estimate that $P_{\rm active}$ ranges within ~ 0.01–1.

Third, the breakout emission needs to be bright enough to overshine the host AGN emission and be detected by current (and future) facilities. However, the probabilities that the breakout emission is brighter than the host AGN emission ($P_{\rm bright}$) and can be detected by facilities ($P_{\rm det}$) are uncertain and difficult to constrain theoretically, as the luminosity is influenced by several uncertain parameters (such as $\epsilon_{\rm B}$, $\epsilon_{\rm e}$, $f_{\rm acc}$, and $\rho_{\rm AGN}$), and transients with a high shock Lorentz factor ($\gamma_{\rm sf,f}$), as suggested for GW150914-GBM, are less likely by a factor of $\sim \gamma_{\rm sf,f}^2$ to be in the beaming direction of the shock. On the other hand, gravitational-wave emission for on-axis events is stronger, which enhances the detection rate of gravitational waves associated with electromagnetic emission beamed in our direction, assuming that the direction of the jet (and the spin of the merger remnant) is perpendicular to the orbital plane of the merging binary.

Finally, black hole mergers need to occur in AGN disks. Although this probability ($P_{\rm AGN}$) has been highly debated (Gayathri et al. 2023), it has been less constrained and ranges from zero to 1.

Considering these factors and adopting the fiducial values for $P_{\rm col}$ and $P_{\rm active}$ and $P_{\rm bright} P_{\rm det} P_{\rm AGN} = 1$, the probability for observing breakout emission associated with mergers in AGN disks is $P_{\rm association} \sim P_{\rm col} P_{\rm active} P_{\rm bright} P_{\rm det} P_{\rm AGN} \sim 0.02$ $(P_{\rm col}/0.7)$ $(P_{\rm active}/0.03)$ $(P_{\rm bright} P_{\rm det} P_{\rm AGN}/1)$. According to this estimate, if one to nine transients, possibly including seven optical (Graham et al. 2023) and two gamma-ray flares (Bagoly et al. 2016; Connaughton et al. 2016), are actually associated with the mergers among O(90) mergers discovered by LIGO/Virgo/KAGRA, as modeled above, $P_{\rm bright} P_{\rm det} P_{\rm AGN}$ can be constrained to be high ($\gtrsim 0.5$). Note that there are significant uncertainties, as $P_{\rm col} P_{\rm active}$ ranges from 4×10^{-3} to 1, and $P_{\rm bright}$, $P_{\rm det}$, and $P_{\rm AGN}$ range from zero to 1, as discussed above. Nevertheless, we expect that future observations, such as by the Vera Rubin Observatory and Roman Space Telescope, will significantly increase $P_{\rm det}$, especially for dimmer breakout emission from less bright AGNs, as well as constrain $P_{\rm col} P_{\rm active}$, $P_{\rm bright}$, and $P_{\rm AGN}$ due to their high sensitivity and wide field of view.

4.2. Possible Obscuration by a Dust Torus

If abundant dust exists along the line of sight to the observer, emission in the optical to soft X-ray bands can be absorbed. Due to the existence of a dust torus around AGNs, the breakout emission in these bands may be largely absorbed. In particular, our model predicts a merger at $R \sim 2.5$ pc for ZTF 19abanrhr, which is beyond the dust sublimation radius ($\sim$0.1 pc for the AGN luminosity of $\sim 10^{44}\,{\rm erg\,s^{-1}}$ in the ultraviolet bands; Barvainis 1987), suggesting the existence of dust in this region. On the other hand, for $R \sim$ a few parsecs, dust in regions above and below the AGN disk plane is possibly cleared out by AGN disk winds (Wada et al. 2016) and/or supernova feedback (Wada et al. 2009; see also observations in Stalevski et al. 2017). If this is the case, the dust in the disk is usually confined to the disk plane and can be evaporated locally by the cocoon feedback, as also confirmed in gamma-ray bursts (Waxman & Draine 2000). The breakout emission can therefore emerge without obscuration by dust in this case. Conversely, the measured properties (e.g., normalization and reddening) of the breakout emission from $R \sim$ a few parsecs may be useful to understand the geometry of dust tori. Also, if the breakout emission is produced from black holes in type II AGNs, unlike the host of ZTF 19abanrhr, the emission in the optical and soft X-ray bands is likely obscured. Since the emission is unobscured in the infrared and hard X-ray bands even if the emission is produced in geometrically thick dust tori, simultaneous observations with infrared/hard X-ray and optical bands will be able to constrain the configuration of dust tori. Thus, wide-field infrared/hard X-ray facilities, such as Swift BAT, will play important roles in finding the electromagnetic counterparts produced in dust tori. Additionally, due to the obscuration, $P_{\rm association}$ is reduced by the covering fraction of the dust torus. Although the influence of dust is uncertain, our model can avoid the issue of dust obscuration to explain ZTF 19abanrhr for the reasons discussed above.

4.3. Parameter Dependence

Figure 6 shows the parameter dependence of the properties of breakout emission, as shown in Figure 2 for the fiducial model. For low $\dot{M}_{\rm in}$ (orange and blue lines) or $f_{\rm acc}$ (red lines), the accretion rate onto the black hole is rather low, which lowers $L_{\rm j}$, $L_{\rm sh}$, and $L_{\rm breakout}$ (panel (c)). At large R, for low $\dot{M}_{\rm in}$ (orange lines), the luminosity is higher than that of the fiducial model. This is because for low $\dot{M}_{\rm in}$, the AGN disk becomes geometrically thin in the outer regions, in which the jet head is less decelerated before the breakout because the jet sweeps up a smaller amount of gas. This enables a higher speed for the shock. Note that the AGN disk density in the outer regimes, where the Toomre parameter satisfies $\sim$1, only depends on the orbital frequency and is unaffected by $\dot{M}_{\rm in}$ (see Equation (3) of Thompson et al. 2005). Although there is the exception as explained above, to produce bright emission (high $L_{\rm sh}$), high $\dot{M}_{\rm in}$ and/or high $f_{\rm acc}$ are indeed required.

The fiducial model parameters and their influence on the properties of the breakout emission are listed in Table 1. There are several sensitive parameters: R, $f_{\rm acc}$, $\epsilon_{\rm B}$, and $\epsilon_{\rm e}$. Here $L_{\rm break}$ is significantly influenced by all four parameters, while $t_{\rm delay}$ and $t_{\rm duration}$ are mostly influenced by R. According to our model, R can be constrained from the timescales, while $f_{\rm acc}$, $\epsilon_{\rm B}$, and $\epsilon_{\rm e}$ can be constrained if nonthermal emission is observed at multiple wavelengths.

4.4. Merging Location

We have proposed that black hole mergers at $R \gtrsim$ pc, $R \sim 10^{-4}$ pc, and $R \lesssim 10^{-4}$ pc can explain the properties of the transients possibly associated with GW190521, GW150914, and LVT151012, respectively. Here we discuss whether such diversity in the positions of mergers in AGN disks is expected. Mergers have been predicted to be concentrated in gap-forming regions (Tagawa et al. 2020b, 2021a) and migration traps (Secunda et al. 2019; McKernan et al. 2020; Yang et al. 2020) in the inner AGN disk or in the outer regions (Perna et al. 2021b) of the disk (but may also occur throughout the disk; McKernan et al. 2020), which have a similar influence on the evolution and mergers of black hole binaries. Gaps are predicted to form for massive black holes or in a thin disk (Tagawa et al. 2020b), while migration traps may form at $\lesssim 10^3\,R_{\rm g} \sim 10^{-4}\,{\rm pc}\,(M/2 \times 10^6\,M_\odot)$ (Bellovary et al. 2016; but see Pan & Yang 2021), where $R_{\rm g} = GM/c^2$, where G is the gravitational constant, and c is the speed of light. If heating torques are taken into account for the dynamics of gas around black holes (Hankla et al. 2020), they can reverse the direction of migration at various distances from the supermassive black hole, while the evolution may be further complicated due to shocked bubbles (Tagawa et al. 2022). Also, the migration timescale without gaps is longer in the outer regions, especially around more massive supermassive black holes (Pan & Yang 2021), in which mergers are also expected at $R \gtrsim$ pc (Perna et al. 2021b). As ZTF 19abanrhr is believed to be associated with an AGN powered by a supermassive black hole of $M \sim 10^8\,M_\odot$, inefficient migration (possibly due to long migration timescales, gaps, or heating torques) may be consistent with mergers at $R \gtrsim$ pc. Also, the mergers at $R \lesssim 10^{-4}$ pc, suggested for the transients possibly associated with GW150914 and LVT151012, may be consistent with mergers in migration traps of AGN disks around less massive supermassive black holes with $M \sim 10^5$–$10^6\,M_\odot$. Conversely, if these transients are actually associated with merging black holes in AGN disks, this places constraints on the positions of gap-forming regions and/or migration traps and yields information on the AGN disks from the properties of the transients.

Since transients are reported for massive mergers (including GW190521) or early events (GW150914 and LVT151012), the detection of transients may require mergers of massive black holes and/or mergers at close distances from us. Indeed, the breakout luminosity ($L_{\rm breakout}$), jet power ($L_{\rm j}$), and accretion rate onto a black hole ($\dot{m}$) depend on the mass of the merged remnant (m) as $L_{\rm breakout} \propto L_{\rm j} \propto \dot{m} \propto m^{2/3}$ (Equation (1) of Tagawa et al. 2022), and the flux is higher for closer events. Also, for transients with a longer delay ($t_{\rm delay}$), such as ZTF 19abanrhr, enhancement of the accretion rate due to recoil kicks (Appendix B) can be expected for massive remnants,

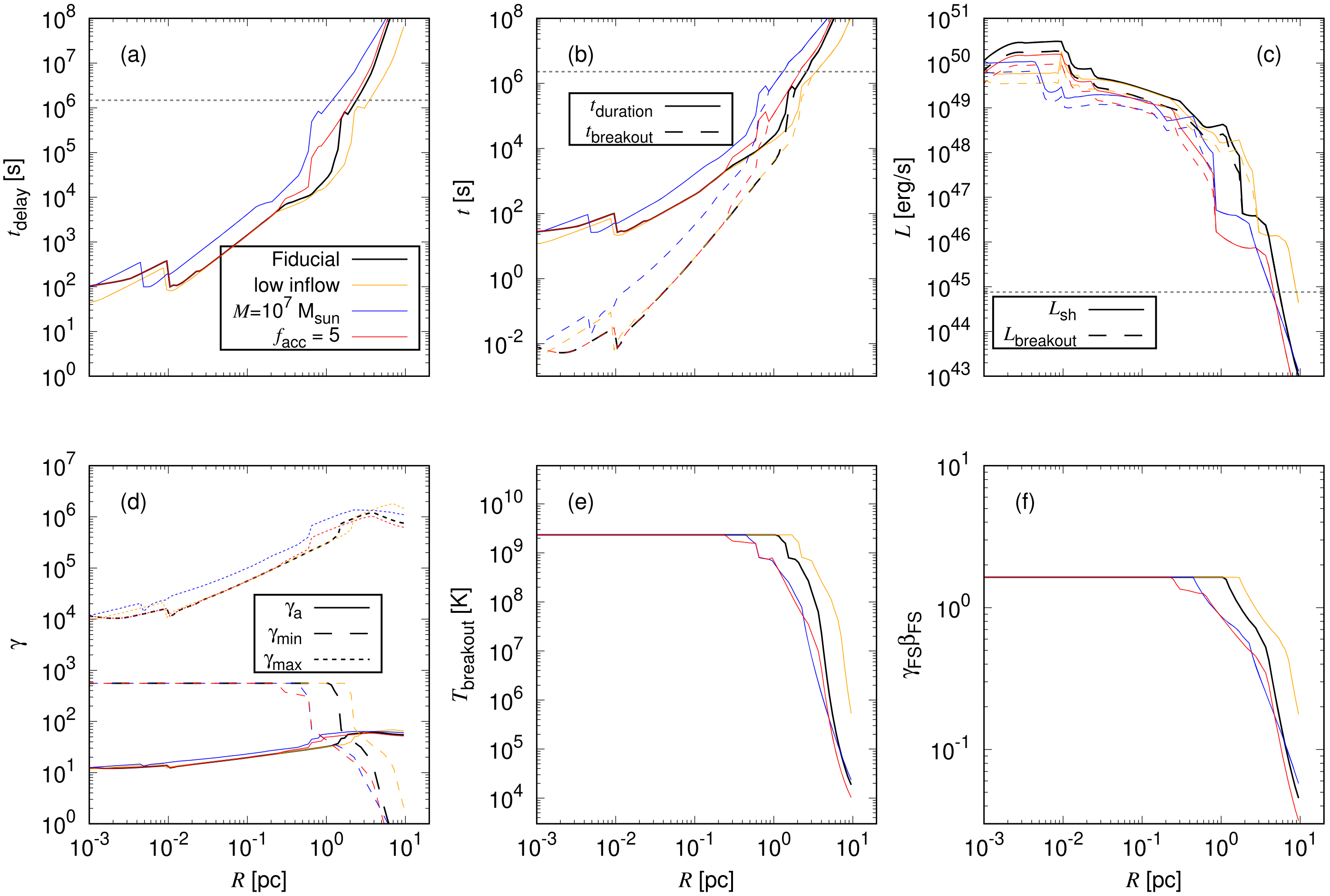

Figure 6. Similar to Figure 2, but results for several choices of the parameters are shown. Black, orange, blue, and red lines, respectively, present results for the fiducial model and the models with $\dot{M}_{\rm in} = 2\,M_\odot\,{\rm yr}^{-1}$, $M = 10^7\,M_\odot$ and $\dot{M}_{\rm in} = 1\,M_\odot\,{\rm yr}^{-1}$, and $f_{\rm acc} = 5$. (a) Delay time. (b) Duration (solid) and breakout timescale (dashed). (c) Shock (solid) and breakout (dashed) luminosities. (d) Absorption (solid), minimum (dashed), and maximum (dotted) Lorentz factors for nonthermal electrons. (e) Breakout temperature. (f) Dimensionless forward shock velocity ($\gamma_{\rm FS}\beta_{\rm FS}$).

since the circum–black hole disk mass within some radius r from the black hole is $m_{\rm CBD}(<r) \propto m^{11/5}$ (Haiman et al. 2009).

5. Summary

In this paper, we investigate the properties of the electromagnetic emission associated with black hole mergers in AGN disks. Both thermal and nonthermal radiation is produced by shocks through collisions between the AGN disk gas and a Blandford–Znajek jet powered by the merger remnant black hole in a direction reoriented at the merger. We suggest that the emission emerging as the jets break out from the optically thick AGN disk can self-consistently account for several features of the tentative electromagnetic counterparts for the three gravitational-wave events ZTF 19abanrhr, GW150914-GBM, and LVT151012-GBM. In particular, the model accounts for the luminosity in the optical bands, as well as the timing and duration of the emission. Our main results are summarized as follows.

1. For mergers at a few parsecs from the central supermassive black hole, the properties of ZTF 19abanrhr are reproduced by nonthermal emission. In this event, the accretion rate onto the black hole is predicted to be enhanced by shocks due to recoil kicks.
2. For mergers closer in vicinity to the central supermassive black hole, the properties of GW150914-GBM and LVT151012 are reproduced by thermal emission.
3. The variety of distances from the central supermassive black hole at which mergers are predicted to take place is consistent with predictions of models for the AGN disk-embedded black hole population, in which the black holes migrate slowly and produce frequent mergers.

To confirm this scenario, discoveries of electromagnetic counterparts for future gravitational-wave events are highly desired. Then, a smoking-gun signature, i.e., bright infrared and X-ray emission concurrent with the optical transient, can be detected by WISE, JWST, Chandra, XMM-Newton, NuSTAR, and FORCE once the host galaxies are localized by optical observations, and/or Swift BAT could be able to detect the breakout emission. If the scenario is confirmed, these systems will be highly useful to improve our understanding of the evolution of compact objects in AGN disks, the structure of AGN disks, plasma physics, and the expansion history of the universe by helping to constrain the Hubble constant, in addition to unveiling the origin of black hole mergers.

This work was financially supported by Japan Society for the Promotion of Science (JSPS) KAKENHI grant Nos. JP21J00794 (H.T.) and 22K14028 (S.S.K.). S.S.K.

acknowledges the support by the Tohoku Initiative for Fostering Global Researchers for Interdisciplinary Sciences (TI-FRIS) of MEXT's Strategic Professional Development Program for Young Researchers. Z.H. was supported by NASA grant NNX15AB19G and NSF grants AST-2006176 and AST-1715661. R.P. acknowledges support by NSF award AST-2006839. I.B. acknowledges the support of the Alfred P. Sloan Foundation and NSF grants PHY-1911796 and PHY-2110060.

Appendix A
Notation

The notations of the variables are listed in Table 2.

Table 2
Notation

Symbol	Description	Symbol	Description
r	Distance from the stellar-mass black hole	$H_{\rm AGN}$	Scale height of the AGN disk
$r_{\rm b}$, $r_{\rm ub}$	Radius within which all gas in a circum–black hole disk is bound and beyond which all gas is unbound after the recoil kick	$r_{\rm acc}$	Radius at which gas accretes onto the stellar-mass black hole on the breakout timescale
$R_{\rm g}$	Gravitational radius of a supermassive black hole GM/c^2	$r_{\rm k}$	Gravitational radius after a recoil kick $Gm/v_{\rm rk}^2$
$d_{\rm L}$, $d_{\rm L,3Gpc}$	Luminosity distance to the source and in units of 3 Gpc	$\Delta_{\rm shell}(\gamma)$	Shell width of electrons with γ emitting nonthermal photons
$d_{\rm edge}$, $d_{\rm edge,BO}$	Distance to the surface of the AGN disk and breakout emission	$R_{\rm out}$	Outer boundary of the AGN disk
m	Mass of the merged remnant black hole	$m_{\rm CBD}(r)$	Mass of the circum–black hole disk within r from a stellar-mass black hole
$\dot{m}$, $\dot{M}$	Accretion rate onto a stellar-mass and supermassive black hole	$m_{\rm BHL}$	Bondi–Hoyle–Lyttleton rate
$\dot{m}_{\rm Edd}$, $\dot{M}_{\rm Edd}$	Eddington accretion rate onto a stellar-mass and supermassive black hole	$l_{\rm Edd}$, $L_{\rm Edd}$	Eddington luminosity of a stellar-mass and supermassive black hole
L, νL_ν	Luminosity and luminosity at frequency ν	$L_{\rm j}$	Kinetic luminosity of the jet
$L_{\rm sh}$	Kinematic power of the shock in the jet head	$L_{\rm breakout}$, $L_{\rm nonthermal}$	Breakout luminosity by thermal emission and nonthermal emission at its peak frequency
$\tilde{L}$	Ratio between the energy density of the jet and the rest-mass energy density of the surrounding medium	$L_{\rm syn}$	Luminosity of synchrotron emission
$\eta_{\rm j}$	Conversion efficiency of mass to the jet	$\eta_{\rm rad}$	Conversion efficiency of mass to radiation in an accretion disk
$Y_{\rm SSC}$, $Y_{\rm 2ndIC}$	Powers of synchrotron self-Compton and second-order inverse Compton scattering compared to that of synchrotron emission	$E_{\gamma,\rm BO}$	Energy of a photon
$t_{\rm duration}$, $t_{\rm delay}$	Duration and delay time of a transient	$t_{\rm break}$,$t_{\rm break,rel}$, $t_{\rm GW,\ break}$	Breakout timescale of a nonrelativistic and relativistic shock and gravitational wave
$t_{\rm diff}$	Diffusion timescale of photons out of the disk	$t_{\rm ang}$	Angular timescale
$t_{\rm dyn,CBD}(r)$	Dynamical timescale of a circum–black hole disk at r	$t_{\rm vis}(r)$, $t_{\rm vis,sh}(r)$	Viscous timescale of a circum–black hole disk at r before and after a shock arises due to a recoil kick
$t_{\rm int}$	Integration time of observations	$t_{\rm arr}$	Timescale for a black hole arriving outside a cavity
$t_{\rm sph}$	Time of transition between the planar and spherical geometries of the breakout shell	$t_{\rm dyn}$	Dynamical timescale of a shell
$t_{\rm trans}$	Transparent timescale	$T_{\rm breakout}$	Breakout temperature
$\gamma_{\rm FS}$, $\gamma_{\rm sf}$, $\beta_{\rm FS}$, $\beta_{\rm sf}$	Lorentz factor of the forward shock and shocked fluid and their dimensionless velocity	$\gamma_{\rm FS,f}$, $\gamma_{\rm sf,f}$, $\beta_{\rm FS,f}$, $\beta_{\rm sf,f}$	Final Lorentz factor of the forward shock and shocked fluid and their dimensionless velocity
$\gamma_{\rm e}$	Lorentz factor of an electron	$\gamma_{\rm m}$, $\gamma_{\rm max}$, $\gamma_{\rm a}$, $\gamma_{\rm c}$	Minimum, maximum, absorption, and cooling Lorentz factors
ν	Frequency of a photon	$\nu_{\rm syn}$, $\nu_{\rm m}$, $\nu_{\rm max}$, $\nu_{\rm a}$,$\nu_{\rm m,SSC}$, $\nu_{\rm a,SSC}$	Synchrotron frequency for electrons with $\gamma_{\rm e} = 1$, $\gamma_{\rm m}$, $\gamma_{\rm max}$, and $\gamma_{\rm a}$ and synchrotron self-Compton frequency for $\gamma_{\rm m}$ and $\gamma_{\rm a}$
$a_{\rm BH}$	Dimensionless spin parameter of a black hole	$a_{\rm BH,rem}$, $a_{\rm BH,iso}$	Dimensionless spin parameter of a merged remnant and an isolated black hole
$f_{\rm acc} = \dot{m}/\dot{m}_{\rm BHL}$	Enhancement factor of the accretion rate of the captured gas	$f_{\rm ext}$	Fraction that the cocoon proceeds to the r-direction after the breakout
$P_{\rm col}$	Probability that a jet launched from a merged remnant collides with unshocked gas	$P_{\rm active}$	Probability that a merged remnant is accreting immediately after merger

Table 2
(Continued)

Symbol	Description	Symbol	Description
P_{bright}, P_{det}, P_{AGN}	Probability that the breakout emission is brighter than the host AGN emission, that can be detected by facilities, and that black hole mergers occur in AGN disks	v_{rk}	Recoil velocity due to anisotropic emission of gravitational waves at merger
f_{b}, f_{ub}	Factors for recoil kicks $f_{\mathrm{b}} = r_{\mathrm{b}}/r_{\mathrm{k}}$, $f_{\mathrm{ub}} = r_{\mathrm{ub}}/r_{\mathrm{k}}$	f_{accum}	Fraction of gas within r_{ub} accumulated within r_{b} after the recoil kick
f_{inc}	Factor that the gas mass within r_{b} is enhanced by the recoil shock	f_{beaming}	Beaming factor taking into account an angular effect
f_{corr}	Correction factor from the total luminosity to the luminosity at some frequency	f_{var}	Ratio of the variable luminosity compared to the average luminosity at some frequency
$P_{\mathrm{association}}$	Probability that black hole mergers in AGN disks accompany electromagnetic observations	i	Inclination angle between the jet and the orbital angular momentum of the AGN disk
θ_{j}, θ_0	Jet opening angle and that at injection	θ_{rk}	Angle of the recoil kick with respect to the plane of the circum–black hole disk
θ_{c}	Opening angle of the cocoon	τ	Optical depth of the AGN disk
κ_{CBD}, κ_{AGN}	Opacity of the circum–black hole and AGN disks	α_{CBD}	Viscous parameter for the circum–black hole disk
ρ_{AGN}, n_{AGN}	Density and number density of the AGN disk	ρ_{sf}	Density of the shocked material
e_{sf}	Energy density of the shocked material	B_{sf}	Magnetic field of the shocked material
ξ	Parameter representing the ratio of the mean free path to the Larmor radius of electrons	τ_q, q, γ_1, γ_2, n_{norm}, C_q	Parameters for the optical depth by synchrotron self-absorption
θ_{PA}	Pitch angle between the magnetic field and the velocity of electrons	p	Power-law slope for injected electrons accelerated by the first-order Fermi process
$N(\gamma)d\gamma$	Number of electrons at $\gamma_e = \gamma \pm d\gamma/2$	p_{dm}	Power-law slope for the mass profile of the circum–black hole disk
s	Power-law slope for electromagnetic radiation at some frequency	e	Elementary charge
c	Speed of light	G	Gravitational constant
k_{B}	Boltzmann constant	h	Planck constant
m_{p}	Proton mass	a	Radiation constant

Appendix B
Enhancement of the Accretion Rate onto Merger Remnants

For accretion onto merged remnants, the accretion rate can be significantly affected by the recoil kicks due to anisotropic radiation of gravitational waves. We follow Rossi et al. (2010) for estimating the enhancement of the accretion rate below. After the recoil kick, all gas in an accretion disk remains bound within a radius of

$$r_{\mathrm{b}} = f_{\mathrm{b}}\, r_{\mathrm{k}} = \frac{f_{\mathrm{b}}\, Gm}{v_{\mathrm{rk}}^2} = 5 \times 10^{12}\ \mathrm{cm}\left(\frac{f_{\mathrm{b}}}{0.2}\right)\left(\frac{m}{150\, M_\odot}\right)\left(\frac{v_{\mathrm{rk}}}{300\ \mathrm{km\ s^{-1}}}\right)^{-2}, \quad \text{(B1)}$$

while all gas is unbound beyond a radius of

$$r_{\mathrm{ub}} = f_{\mathrm{ub}}\, r_{\mathrm{k}}, \quad \text{(B2)}$$

where $r_{\mathrm{k}} \equiv Gm/v_{\mathrm{rk}}^2$, $f_{\mathrm{b}} = [-\cos\theta_{\mathrm{rk}} + (\cos\theta_{\mathrm{rk}}^2 + 1)^{1/2}]^2$, and $f_{\mathrm{ub}} = [\cos\theta_{\mathrm{rk}} + (\cos\theta_{\mathrm{rk}}^2 + 1)^{1/2}]^2$ are the factors related to the kick direction (e.g., $f_{\mathrm{b}} \sim 0.2$ and $f_{\mathrm{ub}} \sim 5$ for $\theta_{\mathrm{rk}} = 30°$), and θ_{rk} is the angle of the recoil kick with respect to the plane of the circum–black hole disk. After the recoil, the accretion onto the black hole is expected only from the circum–black hole disk within the radius r_{ub}. For gas initially within r_{ub}, the angular momentum is rearranged by the kick, and its energy is lost due to shocks within the circum–black hole disk. The fraction of gas within r_{ub} accumulated within $\sim r_{\mathrm{b}}$ after the recoil kick (f_{accum}) is found to be $f_{\mathrm{accum}} \sim 20\%$–$50\%$. Here $\sim 20\%$ is roughly derived from the enhancement of the surface density within r_{b} in Figure 19 of Rossi et al. (2010), while $\sim 50\%$ is roughly derived from the statement that all bound gas falls within r_{b}. Note that in Rossi et al. (2010), a black hole is treated as a sink particle with a size of $0.5 r_{\mathrm{b}}$, within which gas particles are removed from the simulation (which is described in Ponce et al. 2012), which presumably significantly mitigates the surface density in Figure 19 of Rossi et al. (2010). Additionally, Rossi et al. (2010) adopted a more centrally concentrated mass profile of $m_{\mathrm{CBD}}(<r) \propto r^{p_{\mathrm{dm}}}$, with $p_{\mathrm{dm}} = 1/2$, while in the gas pressure–dominated region with a fixed opacity, the profile is less centrally concentrated, with $p_{\mathrm{dm}} = 7/5$ (Haiman et al. 2009). In the case of accretion disks, the factor (f_{inc}) by which the gas mass and density within r_{b} are

enhanced by the recoil shock is roughly estimated as

$$f_{\rm inc} \sim \frac{f_{\rm accum}\,[m_{\rm CBD}(<r_{\rm ub}) - m_{\rm CBD}(<r_{\rm b})]}{m_{\rm CBD}(<r_{\rm b})} \sim f_{\rm accum}\,(r_{\rm ub}/r_{\rm b})^{p_{\rm dm}}, \tag{B3}$$

which is up to $\sim 60(f_{\rm accum}/0.5)$ depending on $\theta_{\rm rk}$ for $p_{\rm dm} = 7/5$.

Hence, it is numerically confirmed that the accretion rate can be enhanced by the recoil kick in the following steps. First, the gas in the annulus between $r_{\rm b}$ and $r_{\rm ub}$ is perturbed by the recoil kick, and it immediately experiences shocks. Due to the shock, the gas loses its angular momentum and migrates inward on the dynamical timescale; then, the gas density in the inner regions of the circum–black hole disk and the accretion rate onto the black hole are enhanced.

Without the recoil kick, the accretion mass within $t_{\rm break}$ is $m_{\rm CBD}(< r_{\rm acc})$, where $r_{\rm acc}$ is the radius at which gas accretes onto the black hole on the breakout timescale, $t_{\rm break}$ ($t_{\rm vis}(r_{\rm acc}) = t_{\rm break}$, where $t_{\rm vis}(r)$ is the viscous timescale of the circum–black hole disk at the distance r from the black hole). It is estimated as

$$r_{\rm acc} = 5 \times 10^{12}\,{\rm cm}\left(\frac{t_{\rm break}}{0.1\,{\rm yr}}\right)^{5/7}\left(\frac{m}{150\,M_\odot}\right)^{1/7} \times \left(\frac{\dot{m}c^2/l_{\rm Edd}}{8 \times 10^4}\right)^{2/7}\left(\frac{\alpha_{\rm CBD}}{0.1}\right)^{4/7}\left(\frac{\kappa_{\rm CBD}}{0.4\,{\rm cm}^2\,{\rm g}^{-1}}\right)^{1/7} \tag{B4}$$

for the standard disk in the gas pressure–dominated regime (Haiman et al. 2009), which is expected at $r = r_{\rm acc}$ for the fiducial model but for $f_{\rm acc} = 1$ (the inner regions are estimated to follow a slim disk model, Abramowicz et al. 1988, while the disk at $r = r_{\rm acc}$ follows the standard disk model), where $l_{\rm Edd}$ is the Eddington luminosity of the stellar-mass black hole, $\kappa_{\rm CBD}$ is the opacity of the circum–black hole disk, $\alpha_{\rm CBD}$ is the alpha parameter for the standard disk, and $\dot{m}c^2/l_{\rm Edd} = 8 \times 10^4$ is the value in the fiducial model with $f_{\rm acc} = 1$ at $R = 2.5$ pc. After the recoil kick, the accretion mass within $t_{\rm break}$ is

$$\sim f_{\rm inc}\, m_{\rm CBD}(<r_{\rm b})\frac{t_{\rm break}}{\max[t_{\rm break},\, t_{\rm vis,sh}(r_{\rm b})]}, \tag{B5}$$

where $t_{\rm vis,sh}(r)$ is the viscosity of the circum–black hole disk at r after the recoil shock occurs in the circum–black hole disk, which can be shorter than $t_{\rm vis}(r)$ due to the shock heating and the possible transition to the slim disk (Abramowicz et al. 1988).

When the breakout timescale ($t_{\rm break}$) is shorter than $t_{\rm vis,sh}(r_{\rm b})$, which is satisfied with $v_{\rm rk} \lesssim 300\,{\rm km\,s^{-1}}$ for $m = 150\,M_\odot$ (Equations (B1) and (B4)), the recoil kick does not eject gas that can accrete onto the black hole within the breakout timescale. In this case, using Equation (B5), the accretion rate and, accordingly, the averaged jet luminosity can be enhanced due to the recoil shock by a factor of

$$\sim f_{\rm inc}\frac{m_{\rm CBD}(<r_{\rm b})t_{\rm vis}(r_{\rm acc})}{m_{\rm CBD}(<r_{\rm acc})t_{\rm vis,sh}(r_{\rm b})} \sim f_{\rm inc}\frac{t_{\rm vis}(r_{\rm b})}{t_{\rm vis,sh}(r_{\rm b})} \gtrsim f_{\rm inc}, \tag{B6}$$

where we use the rough relation of $m_{\rm CBD}(<r_{\rm b})/t_{\rm vis}(r_{\rm b}) \sim m_{\rm CBD}(<r_{\rm acc})/t_{\rm vis}(r_{\rm acc})$. In addition, the enhancement of accretion demands that the breakout timescale be longer than the dynamical timescale within which the shocked gas at $r = r_{\rm b}$ can accrete onto the black hole, $t_{\rm dyn,CBD}(r_{\rm b}) < t_{\rm break}$, where

$$t_{\rm dyn,CBD}(r_{\rm b}) = \left(\frac{Gm}{r_b^3}\right)^{-1/2} \sim 8 \times 10^4\,{\rm s}\left(\frac{m}{150\,M_\odot}\right)^{-1/2}\left(\frac{r_{\rm b}}{5 \times 10^{12}\,{\rm cm}}\right)^{3/2}. \tag{B7}$$

The condition ($t_{\rm dyn,CBD}(r_{\rm b}) < t_{\rm break}$) is not satisfied for a short $t_{\rm break}$, such as in the case of GW150914-GBM, where we assume $f_{\rm acc} \sim 1$, while it is satisfied in the case of ZTF 19abanrhr with $v_{\rm rk} \gtrsim 100\,{\rm km\,s^{-1}}$ for $m = 150\,M_\odot$.

On the other hand, when $t_{\rm vis,sh}(r_{\rm b}) < t_{\rm break}$, satisfied in $v_{\rm rk} \gtrsim 300\,{\rm km\,s^{-1}}$ for $m = 150\,M_\odot$, all of the mass within $r_{\rm b}$ accretes, and the accretion rate is enhanced by a factor of $f_{\rm inc} m_{\rm CBD}(<r_{\rm b})/m_{\rm CBD}(<r_{\rm acc})$. In this case, the accretion rate may even be reduced for $r_{\rm acc} \gg r_{\rm b}$ due to the ejection of gas beyond $r_{\rm b}$, which is the case when $v_{\rm rk} \gtrsim 2000\,{\rm km\,s^{-1}}$ for $m = 150\,M_\odot$ (see Equations (B1) and (B4)). Since its effect is uncertain, we assume that the influence on the accretion rate by the recoil shock is effectively taken into account by enhancing or reducing $f_{\rm acc}$.

Here the recoil velocity for GW190521 is preferred to be $\sim 300\,{\rm km\,s^{-1}}$ or around it ($\sim$100–1000 ${\rm km\,s^{-1}}$; Abbott et al. 2020b). Since $t_{\rm vis}(r_{\rm b}) \sim 0.1$ yr is comparable to the $t_{\rm delay} \sim t_{\rm break} \sim 18$ days inferred for ZTF 19abanrhr, we expect that $f_{\rm acc} \sim f_{\rm inc} \gtrsim 1$, which is predicted to be realized unless $v_{\rm rk} \gtrsim 2000\,{\rm km\,s^{-1}}$. Since $f_{\rm acc}$ is an uncertain quantity, when we discuss the association of ZTF 19abanrhr, we treat it as a parameter whose value is adjusted to match the observational data for ZTF 19abanrhr.

Note that shocked gas, highly pressurized due to the high jet power (high $f_{\rm acc}$), does not significantly eject the circum–black hole disk and reduce the accretion rate onto the black hole, since the dependence of the truncation radius of the circum–black hole disk on the accretion rate is weak (with a power-law index of 8/53; Tagawa et al. 2022), where the truncation radius is the radius beyond which the circum–black hole disk is ejected by the cocoon feedback. Also, a hollow cavity, predicted to exist around the majority of the black holes (Kimura et al. 2021; Tagawa et al. 2022), further weakens this effect.

Appendix C
Telescope Specifications

The properties of the telescopes that would be useful for detecting the electromagnetic counterparts predicted by our model are listed in Table 3.

Table 3
The Names and Properties of the Telescopes Appropriate for Detecting Electromagnetic Counterparts

Telescope Name	Photon Energy	Sensitivity (erg s^{-1} cm^{-2})	Field of View (sr)
JWST	$\sim$0.04–2 [eV]	$\sim 10^{-17}$–10^{-15} for $t_{\rm int} \sim 10^4$ s	$\sim 10^{-6}$
WISE	$\sim$0.05–0.4 [eV]	$\sim 10^{-13}$–10^{-12} for $t_{\rm int} \sim 10^4$ s	$\sim 10^{-4}$
Roman Space Telescope (Spergel et al. 2015)	$\sim$0.6–1 [eV]	$\sim 4 \times 10^{-16}$ for $t_{\rm int} \sim 10^4$ s	$\sim$0.6
ZTF (Bellm et al. 2018)	$\sim$1.4–3.1 [eV]	$\sim 10^{-13}$ for $t_{\rm int} \sim 30$ s	0.01
Vera Rubin (Ivezić et al. 2019)	$\sim$1.2–3.9 [eV]	$\sim 10^{-15}$ for $t_{\rm int} \sim 40$ s	0.003
Subaru/HSC (Aihara et al. 2018)	$\sim$1–3 [eV]	$\sim 10^{-16}$–10^{-15} for $t_{\rm int} \sim 10^3$ s	0.0005
Tomo-e Gozen (Sako et al. 2018)	$\sim$1.7–3.4 [eV]	$\sim 2 \times 10^{-13}$ for $t_{\rm int} \sim 100$ s	0.006
Chandra	$\sim$0.2–10 [keV]	$\sim 10^{-14}$ for $t_{\rm int} \sim 2 \times 10^4$ s	6×10^{-5}
XMM-Newton (Jansen et al. 2001)	$\sim$0.4–3 [keV]	$\sim 10^{-14}$ for $t_{\rm int} \sim 10^4$ s	8×10^{-5}
HiZ-GUNDAM (Yonetoku et al. 2020)	$\sim$0.4–4 [keV]	$\sim 10^{-11}$ for $t_{\rm int} \sim 10^4$ s	1.2
Einstein Probe (Yuan et al. 2015)	$\sim$0.5–4 [keV]	$\sim 3 \times 10^{-11}$ for $t_{\rm int} \sim 10^3$ s	1.0
MAXI (Matsuoka et al. 2009)	$\sim$2–30 [keV]	$\sim 7 \times 10^{-11}$ for $t_{\rm int} \sim 6 \times 10^5$ s	0.07
NuSTAR (Harrison et al. 2013)	$\sim$10–30 [keV]	$\sim 10^{-14}$ for $t_{\rm int} \sim 10^6$ s	3×10^{-5}
FORCE (Mori et al. 2016)	$\sim$1–80 [keV]	$\sim 10^{-14}(t_{\rm int}/10^5\ {\rm s})^{-1}$	10^{-5}
Swift BAT (Barthelmy et al. 2005; Tueller et al. 2010)	$\sim$15–150 [keV]	$\sim 10^{-8}(t_{\rm int}/1\ {\rm s})^{-1/2}$	1.4
Fermi GBM (Meegan et al. 2009)	$\sim$8–4000 [keV]	$\sim 10^{-8}$–10^{-6} for $t_{\rm int} \sim 1$ s	$\sim 4\pi$
INTEGRAL SPI-ACS (Winkler et al. 2003)	$\sim$75–2000 [keV]	$\sim 10^{-7}$–10^{-6} for $t_{\rm int} \sim 1$ s	$\sim 4\pi$

ORCID iDs

Hiromichi Tagawa https://orcid.org/0000-0002-5674-0644
Shigeo S. Kimura https://orcid.org/0000-0003-2579-7266
Zoltán Haiman https://orcid.org/0000-0003-3633-5403
Rosalba Perna https://orcid.org/0000-0002-3635-5677

References

Abbott, B. P., Abbott, R., Abbott, T. D., et al. 2016a, PhRvL, 116, 061102
Abbott, B. P., Abbott, R., Abbott, T. D., et al. 2016b, PhRvD, 93, 122003
Abbott, B. P., Abbott, R., Abbott, T. D., et al. 2016c, PhRvL, 116, 241102
Abbott, R., Abbott, T. D., Abraham, S., et al. 2020a, PhRvL, 125, 101102
Abbott, R., Abbott, T. D., Abraham, S., et al. 2020b, ApJL, 900, L13
Abramowicz, M. A., Czerny, B., Lasota, J. P., & Szuszkiewicz, E. 1988, ApJ, 332, 646
Acernese, F., Agathos, M., Agatsuma, K., et al. 2015, CQGra, 32, 024001
Aihara, H., Arimoto, N., Armstrong, R., et al. 2018, PASJ, 70, S4
Akutsu, T., Ando, M., Arai, K., et al. 2021, PTEP, 2021, 05A101
Artymowicz, P., Lin, D. N. C., & Wampler, E. J. 1993, ApJ, 409, 592
Ashton, G., Ackley, K., Hernandez, I. M., & Piotrzkowski, B. 2021, CQGra, 38, 235004
Bagoly, Z., Szécsi, D., Balázs, L. G., et al. 2016, A&A, 593, L10
Barthelmy, S. D., Barbier, L. M., Cummings, J. R., et al. 2005, SSRv, 120, 143
Bartos, I., Kocsis, B., Haiman, Z., & Márka, S. 2017, ApJ, 835, 165
Barvainis, R. 1987, ApJ, 320, 537
Bellm, E. C., Kulkarni, S. R., Graham, M. J., et al. 2018, PASP, 131, 018002
Bellovary, J. M., Mac Low, M.-M., McKernan, B., & Ford, K. E. S. 2016, ApJL, 819, L17
Berger, E. 2014, ARA&A, 52, 43
Blandford, R. D., & McKee, C. F. 1976, PhFl, 19, 1130
Blandford, R. D., & Znajek, R. L. 1977, MNRAS, 179, 433
Blumenthal, G. R., & Gould, R. J. 1970, RvMP, 42, 237
Bromberg, O., Nakar, E., Piran, T., & Sari, R. 2011, ApJ, 740, 100
Budnik, R., Katz, B., Sagiv, A., & Waxman, E. 2010, ApJ, 725, 63
Buonanno, A., Kidder, L. E., & Lehner, L. 2008, PhRvD, 77, 026004
Calderón Bustillo, J., Leong, S. H. W., Chandra, K., McKernan, B., & Ford, K. E. S. 2021, arXiv:2112.12481
Cao, X. 2011, ApJ, 737, 94
Cheng, K. S., & Wang, J.-M. 1999, ApJ, 521, 502
Connaughton, V., Burns, E., Goldstein, A., et al. 2016, ApJL, 826, L6
Connaughton, V., Burns, E., Goldstein, A., et al. 2018, ApJL, 853, L9
Duffell, P. C., Haiman, Z., MacFadyen, A. I., D'Orazio, D. J., & Farris, B. D. 2014, ApJL, 792, L10
Duras, F., Bongiorno, A., Ricci, F., et al. 2020, A&A, 636, A73
Fan, X., & Wu, Q. 2023, ApJ, 944, 159
Fan, Y.-Z., & Piran, T. 2008, FrPhC, 3, 306
Farris, B. D., Duffell, P., MacFadyen, A. I., & Haiman, Z. 2015, MNRAS, 447, L80
Ford, K. E. S., & McKernan, B. 2022, MNRAS, 517, 5827
Fouka, M., & Ouichaoui, S. 2011, ApJ, 743, 89
Frail, D. A., Soderberg, A. M., Kulkarni, S. R., et al. 2005, ApJ, 619, 994
Gao, H., Lei, W.-H., Wu, X.-F., & Zhang, B. 2013, MNRAS, 435, 2520
Gayathri, V., Healy, J., Lange, J., et al. 2022, NatAs, 6, 344
Gayathri, V., Yang, Y., Tagawa, H., Haiman, Z., & Bartos, I. 2021, ApJL, 920, L42
Gayathri, V., Wysocki, D., & Yang, Y. 2023, ApJL, 945, L29
Ghisellini, G., Guilbert, P. W., & Svensson, R. 1988, ApJL, 334, L5
Graham, M. J., Ford, K. E. S., McKernan, B., et al. 2020, PhRvL, 124, 251102
Graham, M. J., McKernan, B., Ford, K. E. S., et al. 2023, ApJ, 942, 99
Greiner, J., Burgess, J. M., Savchenko, V., & Yu, H. F. 2016, ApJL, 827, L38
Grishin, E., Bobrick, A., Hirai, R., Mandel, I., & Perets, H. B. 2021, MNRAS, 507, 156
Hada, K., Doi, A., Wajima, K., et al. 2018, ApJ, 860, 141
Haiman, Z., Kocsis, B., & Menou, K. 2009, ApJ, 700, 1952
Hankla, A. M., Jiang, Y.-F., & Armitage, P. J. 2020, ApJ, 902, 50
Harrison, F. A., Craig, W. W., Christensen, F. E., et al. 2013, ApJ, 770, 103
Ho, L. C. 2008, ARA&A, 46, 475
Ito, H., Levinson, A., & Nakar, E. 2020, MNRAS, 499, 4961
Janiuk, A., Bejger, M., Charzyński, S., & Sukova, P. 2017, NewA, 51, 7
Jansen, F., Lumb, D., Altieri, B., et al. 2001, A&A, 365, L1
Johnson, M. H., & McKee, C. F. 1971, PhRvD, 3, 858
Ivezić, Ž., Kahn, S. M., Tyson, J. A., et al. 2019, ApJ, 873, 111
Kashiyama, K., Murase, K., Horiuchi, S., Gao, S., & Mészáros, P. 2013, ApJL, 769, L6
Kimura, S. S., Murase, K., & Bartos, I. 2021, ApJ, 916, 111
Kitaki, T., Mineshige, S., Ohsuga, K., & Kawashima, T. 2021, PASJ, 73, 450
Kozłowski, S. 2016, ApJ, 826, 118
Levin, Y., & Beloborodov, A. M. 2003, ApJL, 590, L33
Levinson, A., & Nakar, E. 2020, PhR, 866, 1
LIGO Scientific Collaboration, Aasi, J., Abbott, B. P., et al. 2015, CQGra, 32, 074001
Liska, M., Hesp, C., Tchekhovskoy, A., et al. 2018, MNRAS Lett., 474, L81
Liska, M., Tchekhovskoy, A., & Quataert, E. 2020, MNRAS, 494, 3656
Martin, R. G., Nixon, C. J., Pringle, J. E., & Livio, M. 2019, NewA, 70, 7
Matsuoka, M., Kawasaki, K., Ueno, S., et al. 2009, PASJ, 61, 999
Maughan, B. J., & Reiprich, T. H. 2019, OJAp, 2, 9
McKernan, B., Ford, K. E. S., Bartos, I., et al. 2019, ApJL, 884, L50
McKernan, B., Ford, K. E. S., O'Shaugnessy, R., & Wysocki, D. 2020, MNRAS, 494, 1203
Meegan, C., Lichti, G., Bhat, P. N., et al. 2009, ApJ, 702, 791
Milosavljević, M., & Loeb, A. 2004, ApJL, 604, L45
Miralda-Escudé, J., & Kollmeier, J. A. 2005, ApJ, 619, 30
Mori, K., Tsuru, T. G., Nakazawa, K., et al. 2016, Proc. SPIE, 9905, 99051O
Nakar, E., & Sari, R. 2010, ApJ, 725, 904
Nakar, E., & Sari, R. 2012, ApJ, 747, 88
Narayan, R., Chael, A., Chatterjee, K., Ricarte, A., & Curd, B. 2022, MNRAS, 511, 3795
Olano, C. A. 2009, A&A, 506, 1215
Ostriker, J. P. 1983, ApJ, 273, 99

Palmese, A., Fishbach, M., Burke, C. J., Annis, J., & Liu, X. 2021, ApJL, 914, L34

Pan, Z., & Yang, H. 2021, PhRvD, 103, 103018

Panaitescu, A., & Kumar, P. 2001, ApJL, 560, L49

Perna, R., Lazzati, D., & Cantiello, M. 2021a, ApJL, 906, L7

Perna, R., Lazzati, D., & Giacomazzo, B. 2016, ApJL, 821, L18

Perna, R., Tagawa, H., Haiman, Z., & Bartos, I. 2021b, ApJ, 915, 10

Ponce, M., Faber, J. A., & Lombardi, J. C. 2012, ApJ, 745, 71

Ricci, C., Ho, L. C., Fabian, A. C., et al. 2018, MNRAS, 480, 1819

Romero-Shaw, I., Lasky, P. D., & Thrane, E. 2022, ApJ, 940, 171

Romero-Shaw, I., Lasky, P. D., Thrane, E., & Calderón Bustillo, J. 2020, ApJL, 903, L5

Rossi, E. M., Lodato, G., Armitage, P. J., Pringle, J. E., & King, A. R. 2010, MNRAS, 401, 2021

Rybicki, G. B., & Lightman, A. P. 1979, Radiative Processes in Astrophysics (New York: Wiley-Interscience)

Sako, S., Ohsawa, R., Takahashi, H., et al. 2018, Proc. SPIE, 10702, 107020J

Samsing, J., Bartos, I., D’Orazio, D. J., et al. 2022, Natur, 603, 237

Sapir, N., Katz, B., & Waxman, E. 2011, ApJ, 742, 36

Sapir, N., Katz, B., & Waxman, E. 2013, ApJ, 774, 79

Savchenko, V., Ferrigno, C., Mereghetti, S., et al. 2016, ApJL, 820, L36

Secunda, A., Bellovary, J., Mac Low, M.-M., et al. 2019, ApJ, 878, 85

Sironi, L., Spitkovsky, A., & Arons, J. 2013, ApJ, 771, 54

Soldi, S., Beckmann, V., Baumgartner, W. H., et al. 2014, A&A, 563, A57

Spergel, D., Gehrels, N., Baltay, C., et al. 2015, arXiv:1503.03757

Spitkovsky, A. 2008, ApJL, 673, L39

Stalevski, M., Asmus, D., & Tristram, K. R. W. 2017, MNRAS, 472, 3854

Stone, N. C., Metzger, B. D., & Haiman, Z. 2017, MNRAS, 464, 946

Tagawa, H., Haiman, Z., Bartos, I., & Kocsis, B. 2020a, ApJ, 899, 26

Tagawa, H., Haiman, Z., & Kocsis, B. 2020b, ApJ, 898, 25

Tagawa, H., Kimura, S. S., Haiman, Z., et al. 2022, ApJ, 927, 41

Tagawa, H., Kimura, S. S., Haiman, Z., Perna, R., & Bartos, I. 2023, ApJL, 946, L3

Tagawa, H., Kocsis, B., Haiman, Z., et al. 2021a, ApJ, 908, 194

Tagawa, H., Kocsis, B., Haiman, Z., et al. 2021b, ApJL, 907, L20

Tang, Y., Haiman, Z., & MacFadyen, A. 2018, MNRAS, 476, 2249

Tchekhovskoy, A., Narayan, R., & McKinney, J. C. 2010, ApJ, 711, 50

The LIGO Scientific Collaboration, the Virgo Collaboration, the KAGRA Collaboration, et al. 2021, arXiv:2111.03606

Thompson, T. A., Quataert, E., & Murray, N. 2005, ApJ, 630, 167

Trakhtenbrot, B., Ricci, C., Koss, M. J., et al. 2017, MNRAS, 470, 800

Tueller, J., Baumgartner, W. H., Markwardt, C. B., et al. 2010, ApJS, 186, 378

Wada, K., Papadopoulos, P. P., & Spaans, M. 2009, ApJ, 702, 63

Wada, K., Schartmann, M., & Meijerink, R. 2016, ApJL, 828, L19

Wang, J.-M., Liu, J.-R., Ho, L. C., & Du, P. 2021, ApJL, 911, L14

Waxman, E., & Draine, B. T. 2000, ApJ, 537, 796

Winkler, C., Courvoisier, T. J. L., Di Cocco, G., et al. 2003, A&A, 411, L1

Yang, Y., Gayathri, V., Bartos, I., et al. 2020, ApJL, 901, L34

Yonetoku, D., Mihara, T., Doi, A., et al. 2020, Proc. SPIE, 11444, 114442Z

Yuan, W., Zhang, C., Feng, H., et al. 2015, arXiv:1506.07735